INTERANNUAL AND INTERDECADAL RAINFALL VARIATIONS IN THE

HAWAIIAN ISLANDS

A THESIS SUBMITTED TO THE GRADUATE DIVISION OF THE UNIVERSITY OF HAWAI'I IN PARTIAL FULFILLMENT OF THE REQUIREMENTS FOR THE DEGREE OF

MASTER OF SCIENCE

IN

METEOROLOGY

DECEMBER 2003

BY
Huaiqun Chen

Thesis Committee:

Pao-Shin Chu, Chairperson
Tim Li
Thomas A. Schroeder

Acknowledgments

I would like to thank my advisor, Dr. Pao-Shin Chu for his insight and guidance on my thesis research. He taught me how to propose a study, how to treat and solve problems, and how to interpret and present results.

I owe special thanks to the committee Dr. Thomas A. Schroeder and Dr. Tim Li for their precious comments and valuable suggestions. The discussion with them during my thesis research was very helpful.

I appreciate Rebecca Schneider for proofreading. Thanks must go to all my colleagues for their friendship and encouragement. Finally, I would like to give special thanks to my husband, my parents and my sister for their love, understanding and support.

Abstract

The effect of El Niño-Southern Oscillation (ENSO) and Pacific Decadal Oscillation (PDO) on Hawaiian precipitation has been documented by many researchers. In this observational study, the long-term monthly precipitation data are used to examine the combined effect of ENSO and PDO on Hawaiian precipitation. The results are as follows:

(1) The interseasonal, interannual and interdecadal variability are the dominant frequencies of Hawaiian monthly precipitation.

(2) Hawaiian winter rainfall is negatively correlated with PDO and ENSO; however, Hawaiian summer rainfall is positively correlated with PDO and ENSO.

(3) The synergetic match of PDO and ENSO phases (i.e., El Niño/+PDO or La Niña/-PDO) enhances the ENSO-induced Hawaiian rainfall and circulation patterns in the North Pacific, while the opposite match (i.e., La Niña/+PDO, El Niño/-PDO) tends to weaken the ENSO influence on Hawaiian rainfall and circulation patterns.

(4) The preceding Niño 3.4 index and PDO index provide similar information for predicting the following Hawaiian winter precipitation. The potential predictability of winter rainfall is enhanced, when using both the PDO index and the Niño 3.4 index.

Table of Contents

List of Tables

List of Figures

Chapter 1

Introduction

Considerable large-scale interannual variability occurs in the sea surface temperature (SST) of the Pacific, which is called the El Niño-Southern Oscillation (ENSO) cycle (e.g., Bjerknes, 1969; Horel and Wallace, 1981; etc). The ENSO mode in SST is accompanied by atmospheric variability. Characterizing the warm ENSO (El Niño) phase are the anomalously deep Aleutian low, cold western and central North Pacific, as well as anomalous warming in the central and eastern tropical Pacific. The reversed circulation pattern characterizes the cold ENSO (La Niña) phase.

The climate of the North Pacific is affected by the ENSO phenomenon. Part of the ENSO signal generated in the tropical Pacific is propagated north through atmospheric teleconnection. A study by Wallace and Gutzler in 1981 identified four important teleconnection pattern centers in the North Pacific and North American. This teleconnection pattern is termed Pacific/North American (PNA) pattern, which leads to a deepening Aleutian low. The theoretical results indicate that strong teleconection to midlatitudes for the Northern Hemisphere is possible only during winter, when the westerlies extend from middle latitudes into the equatorial troposphere over the region of heat source. The other part of the ENSO signal is also propagated to higher latitudes as coastal-trapped Kelvin waves, which changes the thermal structure and current patterns in the coastal ocean.

In the late 20th century, the low frequency variation of the North Pacific system was uncovered (e.g., Trenberth and Hurrel, 1994; Zhang et al., 1997; Mantua et al., 1997; Minobe and Mantua, 1999). It was named the Pacific Decadal Oscillation or PDO

(Mantua et al., 1997) and the North Pacific Oscillation or NPO (Gershunov and Barnett, 1998). It is referred to the PDO hereafter. The PDO extremes are labeled as either warm (positive) or cold (negative) phase. The spatial patterns associated with the positive (negative) PDO phase are similar to the warm (cold) ENSO phase. However, the PDO climatic signals, unlike those associated with ENSO, persist for 20 to 30 years. Moreover, PDO's climatic signal is more evident in the midlatitudes, in contrast to ENSO's tropical signal.

Both the ENSO and PDO cycles influence Hawaiian winter rainfall. Most of the El Nino winters in Hawaii are dry (Lyons, 1982; Ropelewski and Halpert, 1987; Chu et al, 1989; Chu, 1995). More recently, the negative relationship between Hawaiian winter precipitation and PDO was identified (Mantua et al., 1997).

In order to assess the influence of the ENSO and PDO on Hawaiian winter rainfall, one should be familiar with the basic synoptic patterns responsible for the winter rainfall. Lyons (1982) determined that three synoptic circulation patterns contribute to 78% of the variance of winter rainfall in Hawaii. They are trade wind, subtropical cyclone, and frontal rainband. In addition, the upper tropospheric divergence over the islands can enhance trade wind rainfall (Blumenstock and Price, 1967; Schroeder, 1977).

Horel and Wallace (1981) proposed a mechanism which accounts for the deficient rainfall during El Niño winter. During El Niño winter, associated heating in the tropical atmosphere, the geopotential height at 200 mb is characterized by negative anomalies over the central North Pacific and positive anomalies over the subtropical North Pacific. The North Pacific jet stream is then stronger and southward than normal. Hawaii is located at the anticyclonic flank in a region of subsidence. This circulation pattern would

2

tend to be associated with upper tropospheric convergence, which indicates the reduced trade wind rainfall. The sinking motion anomalies tend to inhibit the development and maintenance of subtropical cyclones over Hawaii, as well as the southeastward propagation of strong frontal systems into the island chain (Taylor, 1984; Chu et al., 1993; Chu, 1995). Several detailed studies (Chu et al., 1993; Chu, 1995) revealed that the upper tropospheric jet stream remains the same latitude but eastward during El Niño winters. Yet, the physical linkage between Hawaiian winter precipitation and PDO is still unknown.

The similar pattern of ENSO and PDO suggests that the slow-evolved PDO patterns can modulate the ENSO-induced patterns. Many studies investigated the PDO's modification on ENSO climatic patterns. Previous works investigating joint ENSO/PDO impacts on U.S. climate have focused on sea level pressure (SLP), precipitation and surface temperature (Gershunov and Barnett, 1998; Gershunov, 1998; Gershunov and Cayan, 1999; Bove, 2000). Results are conflicting, mainly because that the different climatic indices were used.

Gershunov et al. found that during constructive match conditions (i.e., El Niño/+PDO and La Niña/-PDO), the corresponding winter ENSO pattern over the U.S. continent is intensified and more stable, while the opposite match conditions are destructive to the ENSO pattern. Bove (2000), using varied ENSO and PDO indices, obtained distinct results. His results indicate that positive PDO enhances both El Niño and La Niña climate patterns, while negative PDO weakens ENSO climate anomalies.

There is no previous work to quantify rainfall variations in Hawaii caused by climate phenomena associated with both ENSO and PDO. This study will determine the joint

impact of ENSO/PDO extremes on Hawaiian rainfall. As the similar spatial patterns of PDO and ENSO produce similar effects on Hawaiian winter rainfall, we propose a hypothesis that Hawaiian rainfall patterns created by these two phenomena interact, and the synergetic (opposite) match of PDO and ENSO phase enhances (weaken) the ENSO-induced rainfall anomaly patterns over Hawaii.

A forecast study (Chu, 1989) revealed that severe drought over Hawaii during an ENSO winter could be predicted two seasons in advance using simple regression models. For the non-ENSO drought winter, the predictability decreased. Following Chu's study, the potential predictability of Hawaiian winter rainfall is examined using the preceding PDO and ENSO indices.

Chapter 2

Data and Data Processing

2.1 Data

The National Weather Service cooperative stations provide the monthly precipitation data (TD3220) used in this study. The station data can be obtained from the National Climatic Data Center (NCDC) web page. Only the stations with records longer than 20 years are selected. The data period is from 1950 to 2002. In all, there are 272 stations included. Fig. 1 shows the geographic distribution of these stations.

The circulation data used in this study are the NCEP/NCAR reanalysis data on a 2.5° latitude × 2.5° longitude grid. The data include monthly mean horizontal winds, specific humidity and vertical velocity at standard pressure levels. The SST data are from the Reynolds Reconstructed data set, with a resolution of 2° latitude × 2° longitude.

2.2 Climatic Indices

3.2.1 Hawaii Rainfall Index (HRI)

Hawaii rainfall index (HRI) has been used in several studies (Meisner, 1976; Taylor, 1984; Chu, 1989, 1995). This monthly rainfall index, which represents precipitation variations over different climate regions of the Hawaiian Islands, was developed by Meisner (1976). The monthly rainfall data from nine stations (Fig. 1) on each of the three islands (Kauai, Oahu, and the Island of Hawaii) were used to construct the HRI. The stations represent rainfall from varying elevations (i.e., high, medium and low) and varying locations with respect to the trade wind direction (i.e., windward, neutral and

leeward). Because some of the stations are discontinued, recent records from adjacent stations are used. These new stations are denoted by an asterisk (*) in Table 1. All the indices in this study are obtained for the period of 1905-2002.

3.2.2 Pacific Decadal Oscillation Index (PDOI)

The PDO index (PDOI, hereafter) defined by Mantua et al. (1997) is used in this study to characterize the Pacific low-frequency variability, which is available online at http://tao.atmos.washington.edu/pdo/. The PDOI is defined as the leading principal component of the North Pacific monthly SST variability (poleward of 20°N). Positive values of this index describe anomalously cold SST anomalies around 45°N (i.e., positive PDO phase). Several studies found evidence for PDO cycles during the past century. The negative PDO phase prevailed from 1947 to 1976 while the positive PDO phase dominated from 1925 to 1946 and from 1977 to 1999.

3.2.3 North Pacific Index (NPI)

The North Pacific Index (NPI) (Trenberth and Hurrell, 1994), another index of PDO, indicates the strength of the Aleutian low, which is the primary atmospheric forcing for the PDO. The NPI is defined as the area-weighted mean sea level pressure over the region 30°N-65°N, 160°E -140°W (http://www.cgd.ucar.edu/~jhurrell/np.html).

3.2.4 Niño 3.4 Index

Niño 3.4 index was chosen as the ENSO index because it is more representative of ENSO than other indices (Barnston et al. 1997). Here, we used Trenberth's definition of Niño 3.4 index (http://www.cgd.ucar.edu/cas/catalog/climind/TNI_N34/index.html). According to his definition, El Niño (La Niña) occurs if 5-month running means of SST anomalies in the Niño 3.4 region (5°N-5°S,120°-170°W) exceed 0.4°C (-0.4°C) for six

6

consecutive months or more.

In the present study, we consider the relationship of winter and summer rainfall with ENSO and PDO. To consistent with the wet and dry seasons over Hawaii, winter is defined from November to March of the following year (NDJFM), while summer is from May to September (MJJAS). The winter and summer associated with different ENSO/PDO bins are shown in Table 2. In Table 2, the 1952 winter means the winter season from November 1951 to March 1952, and the 1952 summer means the summer season from May to September of 1952.

Chapter 3

Methodology

3.1 11-year Running Mean (5-Month Running Mean)

Because the peak rainy season in Hawaii occurs in winter, and to keep this season intact, we used the water year calendar from July to June of the following year in accordance with the November–March rainy season. The annual precipitation (AP) is obtained by the sum of the monthly precipitation (MP):

$$AP = \sum MP_n \qquad n = -7, -8, \cdots -12, 1, 2, \cdots 6 \qquad (1)$$

where -7 represents July of the preceding year, and 6 represents June of the current year. As an example, the sum of the monthly precipitation from July 1995 to June 1996 is taken as the annual precipitation of 1996.

The large spatial variations of Hawaii precipitation make the comparison of annual precipitation time series between stations difficult. This difficulty is overcome by standardizing the AP time series for each station. The Standardized Annual Precipitation (SAP) time series can be calculated as follows:

$$SAP_y = \frac{\left(AP_y - \overline{AP}\right)}{sd(AP)} \qquad y = 1, \cdots ny \qquad (2)$$

$$sd(AP) = sqrt\left[\frac{\sum_{y=1}^{ny}\left(AP_y - \overline{AP}\right)^2}{(ny-1)}\right] \qquad (3)$$

where y is the year index (e.g., 1996), ny is the total number of years of the time period

8

under consideration, and $sd(AP)$ is the standard deviation of AP.

An 11-year running mean is applied to the SAP time series to remove the high frequency interannual variations. The filtered result is called the Filtered Standardized Annual Precipitation (FSAP). The filtered values of the first and last five years of the time series represent incomplete 11-year average values, which can be defined by the following equations, respectively:

$$FSAP_y = \frac{1}{6+k} \sum_{j=-k}^{5} SAP_{y+j} \qquad k = 0,1,2,3,4 \qquad (4)$$

$$FSAP_y = \frac{1}{6+k} \sum_{j=-5}^{k} SAP_{y+j} \qquad k = 4,3,2,1,0 \qquad (5)$$

while for the other years, it can be given by

$$FSAP_y = \frac{1}{11} \sum_{j=-5}^{5} SAP_{y+j} \qquad (6)$$

The same method is used to calculate the 5-month running mean of HRI to detect the interannual variation of Hawaiian precipitation. The long-term monthly mean and the standard deviation are calculated separately for each of the 12 months. Standardized anomalies are calculated by taking the difference between the individual monthly value and its long-term monthly mean value, and then dividing the difference by the standard deviation for that month.

3.2 Wavelet Analysis

3.2.1 Wavelet Transform

Wavelet analysis is a powerful tool for localizing the temporal frequency change. Using wavelet analysis, one can determine both the dominant modes of variability and

how these modes vary in time. In this study, the Morlet wavelet analysis is employed to detect the Hawaiian rainfall variations.

Various climate research applications of wavelet analysis can be found in Weng and Lau (1994), Lau and Weng (1995), Wang and Wang (1996), and Torrence and Compo (1998). Hereafter the last paper is referred to as TC1998. In the following, the processing of the wavelet analysis is briefly introduced.

Before applying the wavelet analysis, one must choose a mother wavelet function. In this study, we used the Morlet wavelet analysis. The Morlet mother wavelet is defined as follows:

$$\psi(t) = \pi^{-1/4} e^{i\omega_0 t} e^{-t^2/2} \tag{7}$$

where t has units of months, and ω_0 is a constant that defines the width of the Gaussian envelop of the mother wavelet. In the present study, ω_0 is chosen to be 6 (Farge, 1992).

The wavelet transform of a time series x_n, with equal time spacing dt and $n = 0, \cdots, N - 1$ is defined as follows:

$$W_n(s) = \sum_{n'=0}^{N-1} x_{n'} \psi^* \left[\frac{(n' - n) dt}{s} \right] \tag{8}$$

where the N is the length of the time series , (*) indicates the complex conjugate of the mother wavelet, and s is called wavelet scale.

Because the Morlet wavelet function $\psi(t)$ is complex, the results after the wavelet transform $W_n(s)$ is also complex. The transform can be represented by a real part $\Re\{W_n(s)\}$, and an imaginary part $\Im\{W_n(s)\}$. The result can also be represented in

10

terms of amplitude $|W_n(s)|$ and phase $\tan^{-1}[\Im\{W_n(s)\}/\Re\{W_n(s)\}]$, or as a power

spectrum $|W_n(s)|^2$ (TC1998). The real part and the power spectrum are most commonly

used. The real part depicts both the intensity and phase of the signal variation at particular

scales and locations in wavelet domain (time-scale domain). The power spectrum gives

the energy density, which is also called the local power spectrum (Weng and Lau, 1994;

Lau and Weng, 1995).

3.2.2 End Effect

End effects are defined as the error occurring at the beginning and end of the time

domain, when the wavelet transform is applied to a finite-length time series. In order to

avoid 'end effects', a method called cone of influence (COI) is employed (TC 1998). The

COI is the region where edge effects are important, and it is defined as the e-folding time

at each wavelet scale. For Morlet wavelet, it is defined as $\sqrt{2}s$. The COI for a time

series with the length N is:

$$COI(i) = \sqrt{2}sdt(i-1) \qquad\qquad i = 1, \cdots, (n+1)/2 \qquad (9)$$

$$COI(i) = COI(n-k+1) \qquad\qquad i = (n+1)/2 + 1, \cdots, n \qquad (10)$$

3.2.3 Significance Test

The significance of the wavelet amplitude is evaluated by a Monte-Carlo test

(TC1998). The lag-1 correlation coefficient from the observations is used to construct

100,000 Gaussian red-noise time series. The constructed time series can be shown as the

following:

$$x_n = \alpha x_{n-1} + z_n \qquad\qquad\qquad (11)$$

where α is the lag-1 autocorrelation, $x_0 = 0$, and z_n is taken from the Gaussian white

11

noise. The 95th percentile of the wavelet power spectrum for the 100,000 time series provides the 95% confidence level.

3.3 Nonparametric Mann-Whitney Rank-Sum Test

A nonparametric Mann-Whitney rank-sum test is used to evaluate the difference in location between two independent data samples. This test is used because of the small sample size of the data sets, which makes it difficult to assume any theoretical distribution for the data batches. Nonparametric tests do not require such assumptions, so they are appropriate. The Mann-Whitney rank-sum test is one of the classical nonparametric tests. The null hypothesis for this study is that the two data sets come from the same distribution.

Assume we have two batches of sample data, 1 and 2, and n_1 and n_2 ($n = n_1 + n_2$) are the sample size of these two batches, respectively. The rank-sum test statistic means that the rank within the n observations is pooled under the null hypothesis. R_1 and R_2 are defined as the sum of the ranks held by the members of batch 1 and 2, respectively. Let U be the Mann-Whitney statistic:

$$U_1 = R_1 - \frac{n_1}{2}(n_1 + 1)$$
$$U_2 = R_2 - \frac{n_2}{2}(n_2 + 1)$$

(12)

where both U_1 and U_2 carry the same information, since $U_1 + U_2 = n_1 n_2$. The null distribution of the Mann-Whitney U statistic is approximately Gaussian when n_1 or n_2 is moderately large, with

$$\mu_U = \frac{n_1 n_2}{2} \qquad (13)$$

$$\sigma_U = \left[\frac{n_1 n_2 (n_1 + n_2 + 1)}{12} \right]^{1/2} \qquad (14)$$

Once μ_U, σ_U and U_1 are computed, the U statistic at each grid point is transformed into a standard Gaussian variable by the following equation:

$$z = \frac{U_1 - \mu_U}{\sigma_U} \qquad (15)$$

By choosing a particular confidence level of χ^2 such as 99%, (i.e. the two tailed p-value is 0.005), the corresponding z value can be found from the table for *cumulative probabilities for the standard Gaussian distribution*. If the calculated z-value is less than the chosen level, then the null hypothesis is rejected, implying that the data from the two batches are quite different at the specified test level (Chu, 2002).

3.4 Large-Scale Atmospheric Circulations

A composite approach is used for better understanding the physical mechanisms associated with different ENSO/PDO subsets. A brief description of the horizontal circulation used is presented in Section 3.4.1., followed by the vertical circulation (3.4.2.), and the moisture field (3.4.3.).

3.4.1 Low-Level Circulation

To identify the strength and the position of the upper troposphere jet stream during ENSO/PDO subsets, the 200 mb wind field is analyzed. The 1000 mb wind and SST were analyzed to examine circulation patterns associated with different ENSO/PDO phases.

3.4.2 Vertical Motion

Vertical motion is a very important variable to identify deep convection. The horizontal wind (U, V) and negative pressure vertical velocity $(-\omega)$ at 12 standard pressure levels between 1000 mb and 100 mb were plotted to show the difference between composites. The Hawaiian Islands are located between 18°N-23°N and 154.5°W-160°W. The structure of the east-west vertical circulation was obtained by averaging between 15°N and 25°N, and the structure of the north-south vertical circulation was obtained by averaging between 165°W and 150°W.

3.4.3 Moisture Field

Water vapor is another important ingredient for convection. The composite difference of the vertically integrated moisture flux and its divergence is carried out for each ENSO/PDO bin. In general, moisture divergence patterns correspond well with rainfall anomaly composites.

The horizontal moisture flux in units of $[\text{g m (kg s)}^{-1}]$ at any level of the atmosphere can be calculated by

$$w = qV \tag{16}$$

where V is the horizontal wind vector, and q is specific humidity (g kg^{-1}) which is defined as the ratio of the mass of water vapor in a certain volume to the total mass of air in the same volume.

The vertically integrated moisture flux can be computed from the horizontal moisture flux given by

$$Q = \frac{1}{g} \int_{p_1}^{p_2} qV dp \tag{17}$$

14

where the vertical integration was performed for the eight standard atmospheric levels from 1000 mb to 300 mb. The divergence of the vertically integrated moisture flux is calculated by taking the divergence of equation (17) as

$$Q = \frac{1}{g} \int_{P1}^{P2} \nabla \cdot (qV) dp \qquad (18)$$

Chapter 4

Results and Discussions

4.1 Interannual Variability

Fig. 2 shows the 5-month running mean of the HRI and Niño 3.4 index for the period of July 1905-June 2001. An out-of-phase relationship between the Hawaiian rainfall and Niño 3.4 can be identified, which was originally proposed by Walker and Bliss (1932). For most of the El Niño events, indicated by diamonds, rainfall over Hawaii tends to be below normal, while for most of the La Niña events, indicated by triangles, Hawaiian rainfall is above normal. However, some of the El Niño events are marked by abundant rainfall in Hawaii, such as the 1969 El Niño event. Still, extremely dry winters in Hawaii occurred in the La Niña years as well, such as the 1998-2000 La Niña event.

4.2 Decadal Variability

In order to depict the low-frequency rainfall variability, an 11-year running mean is applied to the HRI and the PDOI (Fig. 3a). The interdecadal variations of the HRI and PDOI are easily recognized. All the time series behave in an oscillatory way with a period longer than 20 years, suggesting a quasi-periodic variation of annual precipitation in the Hawaiian Islands.

The negative relationship between the HRI and the PDOI on decadal timescales is evident in Fig. 3a, and is consistent with the result of Mantua et al. (1997). The HRI had two above-normal epochs (i.e. wet periods): one from 1906 to 1923, and the other from 1946 to 1973. A recent period with a negative rainfall anomaly persisted from 1974 to 2001. The PDOI also had two below-normal epochs, during 1913-1922 and during 1946-

16

1977. The positive PDO regimes prevailed from 1923-1945 and from 1978 to the late 1990s. Meanwhile, the positive PDOI values from 1906-1912 are not consistent with the PDO cycles of the previous studies. This is probably due to the incomplete 11-year running mean at each end of the time series. For the same reason, we cannot see the negative PDO phase starting from 2000, as many scientists suggested. For this figure, the HRI seems to follow the same decadal oscillation of the PDOI, except for two periods (1906-1912 and 1924-1945) when an out-of-phase relationship between these two indices breaks down.

The major transitions in the decadal Hawaiian rainfall occur around 1946 and 1974, corresponding well with similar transitions (1946 and 1978) in the decadal signal of PDOI. The slight shift of PDOI transition points compared to the previous study by Mantua et al. (1997) is due to the difference in applying the running mean and the definition of the water year in this study.

To examine whether the above relation holds for other PDO indices, a similar analysis for the North Pacific Index (NPI) (Fig. 3b) is carried out. For easy comparison, the sign of NPI is reversed. It is clear that the two indices of PDO have a high degree of coherent variability on the interdecadal timescale with only a few differences. Further, the positive relationship between HRI and NPI can be identified. Just like the PDOI series, the in-phase relationship between HRI and NPI breaks down during 1924-1946.

The Pearson correlation coefficients among the indices are calculated and given in Table 3. All correlation coefficients are significant at the 5% level. The highest correlation exists between HRI and NPI, suggesting the important influence of the Aleutian low on Hawaiian rainfall. Therefore, it can be concluded that the interdecadal

17

variations of Hawaiian rainfall and those of SST and SLP are part of a large-scale coupled ocean-atmosphere oscillation in the North Pacific.

4.3 Wavelet Analysis

The time series of the monthly anomalous HRI are shown in Fig. 4a. The power spectrum of the wavelet analysis in Fig. 4b reveals a considerable energy in the high-frequency (0.8-2 years and 2.5-7 years) and low-frequency (15-25 years and 45 years) bands. Most of the high frequency signals, reflected as interseasonal and interannual variations, are also confident at the 95% level. The 2.5-7-year and 15-25-year variations correspond to the low-frequency ENSO variation and the PDO variation respectively.

The dominant high-frequency cycle varies with time. A remarkably strong quasi-biennial oscillation (0.8-2 years) persisted for a decade from the mid-1910s to the mid-1920s. This signal then became weaker until the late 1940s. During this period (from the mid-1920s to the late-1940s), the HRI was dominated by the lower frequency oscillation (5-7 years). Since the late 1940s, the quasi-biennial oscillation reintensified and generally increased to a 4-year oscillation by the 1980s. Since the 1990s, the quasi-biennial oscillation has disappeared and has been overtaken by a quasi-decadal variation (5-7 years). The interdecadal variation (15-25 years and 45 years) runs through the entire time period, but the signal is much weaker. The 45-year oscillation is also located in the region of COI.

4.4 ENSO and PDO Effect on Seasonal Precipitation

The HRI is shown to be negatively correlated with PDOI and Niño 3.4 index, however, the previous study is based only on annual rainfall data from 27 stations in the islands. To reveal whether the relationship holds for the seasonal rainfall of the entire

state, two climate stage composites are carried out for the qualified stations (272 stations) in Hawaii: the El Niño minus La Niña composite, and the positive PDO minus negative PDO composite. The difference of each composite is then tested for statistical significance. The nonparametric Mann-Whitney test is applied to evaluate the confidence level of the precipitation difference. The minimum sample size was set at five for each data batch. Because of the incomplete precipitation records, some stations failed to meet this requirement. As such the number of stations used for the significance test is less than that for the corresponding precipitation analysis.

4.4.1 Winter Precipitation Analysis

Figure 5a displays the winter precipitation difference pattern between El Niño and La Niña in terms of standardized anomalies. El Niño is related to dry conditions (negative anomalies) in the entire state, in agreement with previous annual precipitation analysis. Positive values can be seen in the northern tip and the leeward area of the Island of Hawaii, as well as small windward areas in Maui and Molokai.

The composite difference between the positive and negative PDO phases (Fig. 5b) reveals that PDO has the same effect on winter rainfall, though it is much weaker compared to ENSO's effect. Moreover, the dry conditions have less spatial extent compared to the ENSO composite. The area of wet anomalies on the Island of Hawaii expands from the northern tip to southward. This wet condition is also visible in Maui and windward area of Oahu.

The corresponding nonparametric Mann-Whitney test for the two climate stages is shown in Fig. 6. In general, during the ENSO composite, stations exhibit confidence above the 80% level (Fig. 6a). Stations with confidence tend to be at the leeward side of

the islands, especially for the Island of Hawaii, Maui and Oahu. The higher confidence level with spatial coherence can be found on Kauai, Oahu and Lanai. For the other three islands (Molokai, Maui and Hawaii), the significance level is relatively lower. For the PDO composite (Fig. 6b), fewer stations are statistically significant, and the significance level is lower compared to Figure 6a.

4.4.2 Summer Precipitation Analysis

By summer, the winter ENSO rainfall anomaly patterns (Fig. 7a) are no longer present. Summer ENSO rainfall patterns depict wet anomalies in most areas of the entire state, as well as small dry areas on each island. These dry regions include southwest Kauai, southwest Oahu, and leeward and Hilo area of the Island of Hawaii. The summer PDO rainfall pattern (Fig. 7b) is similar to the ENSO pattern (Fig. 7a). The obvious difference is the dry areas in Maui and Lanai. Dry anomalies at the windward side of the Island of Hawaii extend through the saddle between the two volcanic mountains to the leeward area.

The summer ENSO effect on Hawaiian rainfall (Fig. 8a) is less significant compared to the winter ENSO effect, as only a few stations exhibit confidence between the 80-95% levels. This is probably due to the weakness of ENSO events during the summer. The PDO confidence pattern (Fig. 8b) indicates that the wet anomalies are significant over many stations of the entire state, with the highest confidence along the coasts of the Island of Hawaii and the windward coasts of the other islands.

The observational rainfall analyses show that ENSO and PDO have the same effect on seasonal Hawaiian rainfall; however, the effects are different for winter and summer. Dry winters tend to occur during El Niño (positive PDO phase) and wet winters tend to

20

occur during La Niña (negative PDO phase). Wet summers tend to occur during El Nino (positive PDO phase); while dry summers tend to occur during La Niña (negative PDO phase).

4.5 Winter ENSO and PDO Circulation Patterns

The rainfall analyses show the same effect of ENSO and PDO on seasonal Hawaiian rainfall. In this section, the associated atmospheric circulation pattern composites are presented. Only the winter circulation patterns are shown in this section because ENSO has a stronger effect during winter.

According to the mechanism proposed by Horel and Wallace (1981), the 200 mb wind field and the jet stream explain the deficient rainfall during El Niño winters. The 200 mb wind field anomaly for the ENSO composite and PDO composite are given in Fig. 9. The El Niño signal (Fig. 9a) over the North Pacific consists of an anomalous cyclonic circulation in the Gulf of Alaska and an anomalous anticyclonic circulation over the subtropical North Pacific. This anomalous circulation pattern enhances the westerly wind at the midlatitudes. The PDO composite (Fig. 9b) shows similar circulation patterns in the higher latitudes. However, the tropical signals of these two composites are different.

A further examination of 200 mb jet stream (Fig. 10) is shown. According to Chu (1995), the subtropical jet stream core at 200 mb is defined as a region where wind speed exceeds 40 m/s. It is evident that the jet core is slightly eastward during El Niño winters than during La Niña winters (Figs. 10a and 10b). Similar feature is evident in the PDO composite (Figs. 10c and 10d). The jet core is more eastward during positive phases than during negative phases. As a result, Hawaii is located close to the right exit region of the

jet core in an area of upper-level convergence. These features are consistent with the circulation distribution demonstrated in Fig. 9.

The anomaly composite maps of surface winds and sea surface temperature (SST) for two climate stages are shown in Fig. 11. Figure 11a shows the difference between El Niño and La Niña. The anomalous pattern consists of warm SST anomalies stretching from the eastern to western equatorial Pacific, a cool pool centered in the mid-latitude North Pacific, as well as an anomalous cyclonic circulation in the Gulf of Alaska. A band of westerly anomalies is seen to the north of Hawaii, which weaken the easterly trade winds over the North Pacific. Partially because of the weakening of trade winds, drought prevails over Hawaii during El Niño winter. Similar composite patterns are seen in the PDO (Fig. 11b) composites. However the SST signal and the wind pattern in the equatorial Pacific are less pronounced in these composites.

The composite differences of the vertically integrated moisture flux and its divergence for the two climate stages are given in Fig. 12. Both show similar moisture flux patterns and enhanced moisture flux divergence in Hawaii. In Fig. 12a, the divergence of moisture flux prevails over almost the entire western Pacific, extending eastward to the eastern tropical Pacific. For Fig. 12b, however, the divergence belt is confined between 10°N and 30°N and the moisture convergence dominates almost the entire midlatitude North Pacific, corresponding to the less severe drought condition during the positive PDO phase relative to the El Niño phase.

The north-south vertical cross-section composite (Fig. 13) is obtained by averaging the meridional wind component and the negative pressure vertical velocity between 150°W and 165°W. The similar circulation patterns shown in Fig. 13 support our early

rainfall composite results. The north Pacific is dominated by anomalous descending motions from the equator to 30°N, where the Hawaiian Islands (20°N) are located. The shading represents the confidence level based on vertical velocity. In the ENSO composite (Fig. 13a), the vertical velocity over Hawaii is statistically significant; however in the PDO composite (Fig. 13b), it is less evident and only significant at the lower levers.

The structure of the east-west vertical cross-section is also investigated (Fig. 14). The height-longitude structures are obtained by averaging the zonal wind component and negative pressure vertical velocity between 15°N and 25°N. The cross-section in Fig. 14a is characterized by two gigantic cells, associated with broad anomalous sinking motions between 160°E and 160°W and rising motion anomalies at 100°W and in the western Pacific (120°E). Hawaii (160°W-155°W) is located in the region of sinking motions. The obvious difference between the PDO composite (Fig. 14b) and the ENSO composite (Fig. 14a) is the sinking motion anomalies at 100°W in Fig. 14b. The anomalous sinking motions over Hawaii are weaker and only significant at lower levels. Combining both Fig. 13 and Fig. 14, the east-west and north-south circulation have common descending motion anomalies over the central North Pacific.

4.6 PDO's Modulation on ENSO-induced Precipitation

The previous rainfall analyses have focused on the ENSO effect and the PDO effect on seasonal precipitation. To reveal the different PDO phase effect on the ENSO-induced Hawaiian rainfall, precipitation anomalies are examined for each ENSO/PDO subset. The ENSO/PDO cases can be seen as subsets of respective ENSO extremes according to the different phase of PDO. For example, El Niño/+PDO phase is a portion of the entire

El Niño data set; and the entire El Niño data set is composed by El Niño/+PDO and El Niño/-PDO. Each subset is then compared to its respective ENSO-only patterns. Because the weak ENSO effect during summer and the complexity of Hawaiian summer precipitation, the summer precipitation analysis is not conducted. Yet the simple analysis for summer precipitation is listed in Table 2.

To compare the ENSO/PDO anomaly patterns to ENSO-only anomaly patterns (i.e. El Niño or La Niña) requires a standard from which anomalies are compared. Thus, the long-term seasonal mean is employed. Patterns of seasonal anomalies associated with ENSO-only extreme events over Hawaii are obtained by subtracting the long-term seasonal climatology mean from the El Niño (La Niña) seasonal precipitation at each station, and normalizing by the seasonal standard deviation at every station. ENSO/PDO precipitation anomalies are calculated in the same manner as the ENSO-only anomalies. By comparing the precipitation anomalies of a given subset to the corresponding ENSO-only anomaly composite, locations where the PDO has an impact are identified.

4.6.1   PDO's Modulation on Winter El Niño Precipitation

Figure 15a displays the winter El Niño precipitation pattern in terms of standardized anomalies. State-wide dry conditions prevail. Small wet areas can be identified from each island, except Lanai.

The subset composites according to positive and negative PDO phases are shown in Figs. 15b and 15c. During El Niño/+PDO (Fig. 15b), dry conditions are enhanced, compared to Figure 15a. The wet conditions seen in the ENSO-only composite are strongly reduced over the islands. This much drier pattern indicates the constructive effect of positive PDO on El Niño. During the El Niño/-PDO (Fig. 15c), the drought is

less severe, reversing the dry conditions typically seen in El Niño events (Fig. 15a). The wet anomalies prevail, extending from the coast to the center of the islands.

The nonparametric test is employed (Fig. 16). The El Niño-only composite (Fig. 16a) exhibits statistical significance along the coast of Kauai, western Molokai, the southwest portion of Lanai, the leeward coast of Maui and the Island of Hawaii. Relative to this El Niño-only composite, the confidence level in the Hawaiian Islands increases during El Niño/+PDO (Fig. 16b). Areas that are statistically significant nearly spreads island wide for Kauai, Oahu, and Lanai. Confidence can be seen along the coast of Maui, with intervals ranging from 80 to 95 percent. For the Island of Hawaii, leeward areas show significance. During El Niño/-PDO (Fig. 16c), only a few stations reach the confidence level.

4.6.2. PDO's Modulation on Winter La Niña Precipitation

The winter La Niña patterns are dominated by wet anomalies (Fig. 17a). The wet anomalies almost cover the entire state. Compared to the La Niña-only composite, the wet conditions of La Niña/+PDO in Figure 17b are much weaker, showing isolated dry anomalies in each island. The large areas of dry anomalies are observed in the islands of Hawaii, Maui, Lanai and Molokai. Small areas in west Kauai and south Oahu are slightly drier than normal. For the other four islands, the dry conditions are even stronger. The La Niña/-PDO patterns (Fig. 17c) are almost identical to those of La Niña (Fig. 17a), yet, the magnitude of the wet anomalies is higher.

Statistical significance is reached along the coast of Kauai, most areas of Oahu and the Island of Hawaii during the summer La Niña-only composite (Fig. 18a). With the modification of positive PDO (Fig. 18b), the areas of confidence level diminishes, except

25

for Kauai. The confidence pattern of the negative PDO subset (Fig. 18c) is similar to the La Niña-only pattern (Fig. 18a), extended confidence areas on Maui and Lanai, with an intensified confidence level on northern Oahu.

4.7. PDO's Modulation on ENSO Circulations

In this section, the winter ENSO (El Niño and La Niña) composite and sub-composites according to the PDO phase are examined, with the focus on associated Hawaiian winter rainfall patterns.

4.7.1. PDO's Modulation on Winter El Niño Circulations

Fig. 19 displays the 200 mb wind filed anomalies for the winter El Niño composite and subcomposites according to the PDO phases, which corresponds to the rainfall patterns in Fig. 13. The El Niño signal is just similar to Fig. 9a. Further compositing by PDO phase reveals that the anomalous cyclonic circulation in the Gulf of Alaska is intensified during El Niño/+PDO phase (Fig. 19b). By contrast, El Niño/-PDO winters exhibit a rather different pattern. The anomalous cyclonic circulation propagates eastward to the west coast of the North America, and another anomalous cyclonic circulation appears west of Hawaii. It is apparent from the above composites that the high-latitude El Niño signals are enhanced during positive PDO phase, and altered during negative PDO phase. However, the tropical and subtropical El Niño signals remain unchanged or slightly changed.

The mean 200 mb wind fields for each El Niño subset are displayed (Fig. 20). Compared to the mean El Niño jet steam (Fig. 20a), the eastward shift of the jet core (150°W) can be identified during El Niño/+PDO (Fig. 20b), yet the jet core retreats westward (170°E) during El Niño/-PDO (Fig. 20c).

26

The El Niño winter anomalies of surface winds and SST are shown in Fig. 21. A cyclonic circulation anomaly appears in the North Pacific, with a band of westerly anomalies north of Hawaii, which weaken the trade wind over the North Pacific and reduce the trade wind rainfall over Hawaii. The ENSO/PDO composites reveal that the El Niño signal is determined primarily in El Niño winters during the positive PDO phase. During El Niño/+PDO (Fig. 21b), it is evident that the positive PDO enhances the El Niño mode. During these winters, the cyclonic anomalies are enhanced, with stronger westerly anomalies over the midlatitudes. In contrast, the El Niño pattern disappears during El Niño/-PDO phase (Fig. 21c). The North Pacific is dominated by an anticyclonic circulation anomaly, with northeasterly anomalies over the Hawaiian Islands. Thus, the trade wind over Hawaii is enhanced.

The composite differences of the vertically integrated moisture flux and its divergence are given in Fig 22. Although all these panels show enhanced moisture flux divergence in Hawaii, the moisture flux divergence of El Niño/+PDO winters (Fig. 22b) is the most pronounced, stretching across the North Pacific from 10°N to 30°N. It is apparent that the typical El Niño moisture divergence pattern is enhanced during the positive PDO phase. The moisture flux patterns of these three figures are different. The El Niño composite (Fig. 22a) shows an anomalous cyclonic moisture flux near the west coast of North America. Adding the positive PDO phase strengthens (Fig. 22b), this anomalous cyclonic moisture flux cell extends westward to the central North Pacific. Yet, the moisture flux over the Hawaiian Islands of these two composites (Figs. 22a and 22b) is similar. The negative PDO destroys the El Niño pattern in the central North Pacific (Fig. 22c), with an anticyclonic moisture flux cell northwest of the islands. The moisture flux

over Hawaii in this figure is also completely reversed from the previous two figures (Figs. 22a and 22b), with a northwesterly moisture flux persisting over the islands.

The north-south vertical cross-section composite and its nonparametric Mann-Whitney test based on the vertical velocity for three El Niño subsets are shown in Fig 23. The first two composite modes (Figs. 23a and 23b) are similar to each other. The North Pacific is dominated by anomalous descending motions extending from low latitudes northward to at least 30°N. Hawaii is located in an area of strong anomalous descending motion, consistent with the deficit rainfall during these two subsets. Although the sinking motion anomalies are visible around Hawaii in the El Niño/-PDO subset (Fig. 23c), they are weaker and not significant.

The structure of the east-west vertical cross-section is also investigated (Fig. 24), with rising motion anomalies at 120°E and in the East Pacific (100°W), and a broad sinking motion in the central North Pacific. The sinking anomalies are evident in the central Pacific (from 150°E to 150°W) in these three figures; however, the modification by the negative PDO phase (Fig. 24c) makes them less spatially coherent. Sinking motion anomalies over Hawaii are weaker and only significant at mid-levels, resulting in relative wet conditions in Hawaii even during El Niño events (Fig. 15c).

4.7.2. PDO's Modulation on Winter La Niña Circulations

The PDO's modification on the winter La Niña patterns will be discussed, in reference to the rainfall patterns in Fig. 17. The La Niña 200 mb wind anomaly (Fig. 25a) is reversed to the El Niño 200 mb wind field (Fig. 19a). It is characterized by an anomalous anticyclonic circulation in the Gulf of Alaska, and an anomalous cyclonic circulation in the subtropical North Pacific. The La Niña patterns during different PDO phases (Fig.

25b and 25c) reveal that the La Niña 200 mb signal is determined primarily in La Niña winters occurring during the negative PDO phase (Fig. 25c). In contrast, the 200 mb wind field of La Niña/+PDO subset (Fig. 25b) is rather different. The mean 200 mb wind (Fig. 26a) shows that the jet core during La Niña winter extends to 172°W. Considering the effect of PDO phases, the eastern border location of the jet core is slightly changed. During the La Niña/+PDO winters (Fig. 26b), the jet core is eastward to 165°W, yet, it withdraws to 175°W during La Niña/-PDO winters (Fig. 26c).

The La Niña mode (Fig. 27a) is simply a reversal of the El Niño mode, with warm SST anomalies in the North Pacific and cold SST anomalies in the equatorial Pacific, and an anomalous anticylconic circulation in the central North Pacific. During the positive PDO phase, the La Niña pattern (Fig. 27b) is slightly distorted at higher latitudes (poleward of 30°N). As expected, the addition of the negative PDO phase enhances the La Niña pattern (Fig. 27c).

The vertically integrated moisture flux and its divergence composites are shown in Fig. 28. The moisture flux patterns of these three pictures are similar, except for the locations of the anticyclonic moisture flux. The La Niña and La Niña/-PDO patterns (Figs. 28a and 28c) are characterized by an anticyclonic moisture flux in the central North Pacific; during the positive PDO phase (Fig. 28b), this anticyclonic flux is tilted and shifted east to the eastern Pacific. Moisture convergence dominates the Hawaii Islands during La Niña and its negative PDO phase subsets (Figs. 28a and 28c). The moisture divergence patterns during La Niña/+PDO (Fig. 28b) are reversed, with moisture divergence extending from 10°N to 25°N. The state-wide wet pattern is no longer visible during the La Niña/+PDO subset (Fig. 17b).

The north-south vertical circulations are shown in Fig. 29. The composites according the PDO phase reveal that the La Niña height-latitude sections are determined primarily in La Niña/-PDO subset. The similarity of Figures 29a and 29c is evident. They are characterized by rising motion anomalies in the South Pacific (south of 20°S) and North Pacific (north of 12.5°N), as well as descending motion anomalies near the equator. In the Hawaii area, the ascending anomalies are significant at the middle level for La Niña/+PDO subsets (Fig. 29b), and significant at the lower level for La Niña/-PDO subsets (Fig. 29c).

Figure 30 shows the east-west vertical circulation. The La Niña vertical circulation (Fig. 30a) is the reverse of El Niño's (Fig. 24a), with descending motion anomalies at 120°E and in the East Pacific (100°W), as well as the broad ascending motion over the central Pacific (160°E-150°W). Compared to La Niña pattern (Fig. 30a), the significant ascending motion anomalies shrink (180°-160°W) during the La Niña/+PDO subset (Fig. 30b), and extend (150°E-150°W) during the La Niña/-PDO subset (Fig. 30c). As a result, the ascending motion over Hawaii (155°W-160°W) is statistically significant (Figs. 30a and 30c).

4.8. Potential Predictability

The above study about PDO and ENSO modification on Hawaiian seasonal rainfall has shown that ENSO induced rainfall anomalies are significantly enhanced when PDO and ENSO interfere constructively (i.e. El Niño/+PDO or La Niña/-PDO) and are reduced when PDO and ENSO interact destructively. Given this information, I will exam the potential predictability of winter Hawaiian rainfall using information from the PDO and ENSO indices.

The Niño 3.4 index averaged over three summer months (JJA) is the ENSO-associated predictor for the subsequent winter rainfall (NDJFM). Large positive values of Niño 3.4 index are considered to be associated with El Niño, while large negative values are considered to be associated with La Niña. The PDOI is averaged from September of the preceding year to the following August. However, to preserve as much information as possible about the months near the target winter season, different weight is assigned to each of the 12 months. These weights, from September to August, are 1/50, 1/50, 1/50, 1/50, 1/50, 1/20, 1/20, 1/10, 1/10, 1/10, 2/10, 3/10. Hence, the preceding annual PDOI and the summer Niño 3.4 index are used as predictors of the target Hawaiian winter rainfall.

The time series of Hawaiian winter rainfall is divided into terciles. Hawaiian winter rainfall is classified as above normal, normal and below normal. The same method is also applied to Niño 3.4 index and PDOI. The distribution of the N winters can be distributed as a/b/c, where a+b+c=N. Here, "a" indicates the number of dry winters (lower tercile), "b" is the number of winters with near-normal precipitation (middle tercile), and "c" is the number of wet winters (upper tercile). The hypothesis is proposed: the upper tercile of Niño 3.4 and PDO indices is followed by dry winters. The perfect relationship would lead to the following winter precipitation distribution: a/b/c = N/0/0. However, if the Niño 3.4 and PDO indices provide no information on the winter rainfall, then the distribution should be an even event, i.e. a=b=c. Thus, the fraction of each category should be 33%.

The scatterplots for the winter precipitation from 1951-2002 are shown in Fig. 31. The x-coordinate is the JJA Niño 3.4 value, and two vertical dotted lines split the Niño 3.4

31

index into terciles. The y-coordinate is the corresponding Sept-Aug PDOI, and is divided into terciles by two horizontal dotted lines. The target NDJFM precipitation is presented by three different symbols. Xs denote winter precipitations in the middle tercile, open circles represent the below normal winter precipitation (lower tercile), and closed circles stand for the above normal winter precipitation (upper tercile).

The distribution of winter precipitation following the upper tercile Niño 3.4 index is shown at the bottom right outside the figure. The trio of numbers indicates the distribution of dry/median/wet, so a/b/c = 11/3/3 and N = 17. The fraction of dry winters following the above normal Niño 3.4 index is a/N=11/17=65%, which exceeds a non-skill forecast (33%) by 32%. Following the lower tercile Niño 3.4 index, the winter precipitation is distributed as 3/8/6. Thus, the chance of a wet winter following a low Niño 3.4 index is 35%. The above results demonstrate the historically strong El Niño effect on Hawaiian winter precipitation.

Considering the PDO-only effect, the PDOI provides little information about winter precipitation. The above normal PDOI yields an observed distribution of 6/5/4, so that the chance of a dry winter is 40%. Negative PDOI yields no predictive skill at all (4/7/6 yields 35%, with no enhanced probability of a wet winter).

As the Niño 3.4 and PDO indices provide similar information for the winter rainfall prediction, the combined information of PDO and Niño 3.4 indices is taken into consideration, and a better potential predictability of winter precipitation is expected. The trio of numbers at the right corner of Fig. 31 indicates that the distribution of Hawaiian winter rainfall following the upper tercile of the Niño 3.4 and PDO indices is 5/1/1. The fraction of dry winters following above normal Niño 3.4 and PDO indices is

a/N=71%. It is enhanced by 38% over the climatological probability of 33%. The winter precipitation distribution wielded by the lower tercile Niño 3.4 and PDO indices is 2/4/4 (lower left corner). The chance of a wet winter following warm Pacific SSTs (both Niño 3.4 and PDO indices) is 4/10 = 40%.

It can be concluded that the Niño 3.4 index is a better predictor than PDOI for Hawaiian winter precipitation. The combination of Niño 3.4 and PDO indices increases the predictability, especially for dry winter.

Chapter 5

Summary

Using statistical methods, the monthly HRI are analyzed. The results show significant interseaonal, interannual and interdecadal variations of monthly precipitation. Hawaii tends to be dry (wet) during most El Niño (La Niño) events. The annual Hawaiian rainfall is negatively correlated with the PDOI, with the correlation coefficients being significant at the 5% level. A composite analysis based on 272 rain gages reveals that this negative correlation with PDO and ENSO exists only during the winter. In contrast, Hawaiian summer rainfall is positively correlated with PDO and ENSO.

To reveal the PDO modification on ENSO, the rainfall analysis of various ENSO/PDO subsets are examined for winter and summer, and compared to those of ENSO-only subsets. The results display that the constructive match of ENSO and PDO (i.e. El Niño/+PDO and La Niña/-PDO) enhances the related ENSO rainfall patterns in Hawaii, while the destructive match (i.e. El Niño/-PDO and La Niña/+PDO) weakens the ENSO influence on Hawaiian rainfall.

The associated winter large-scale atmospheric circulations demonstrate the similarity of the ENSO and PDO atmospheric patterns. During the El Niño and positive PDO phase, an anomalous surface cyclonic circulation cell dominates to the north of Hawaii, with westerly anomalies over the islands. This pattern reduces the trade wind strength and trade wind rainfall over Hawaii. The 200 mb jet stream is stronger and eastward, thus Hawaii is situated at the anomalous anticyclonic flank in a region of subsidence. Anomalous sinking motions appear in the central North Pacific in the east-west and north-south vertical circulation composites. Sinking motion anomalies lead to low-level

divergence and reduced convection over Hawaii. Due to persistent descending motion anomalies, synoptic systems such as kona storms and midlatitude frontal rainbands that usually produce rainfall in the Hawaiian Islands become unfavorable and drought tends to occur. In addition, the associated vertically integrated moisture flux divergence provides adverse conditions for convection to occur. The winter circulations associated with the ENSO/PDO subsets are explored. Results indicate that similar matches enhance relative ENSO atmospheric circulations, while opposite matches tend to cancel each other.

The PDO is shown to have strong effects on the ENSO patterns, and the ENSO index (SOI) has been employed as a predictor for Hawaiian winter precipitation (Chu, 1989). Thus one must consider both ENSO and PDO effects to obtain better potential predictability. Results of the study indicate a pronounced increase of forecast ability compared to ENSO-based and PDO-based forecasts. When the Niño 3.4 and PDO indices reach extreme positive values prior to the rainy season, dry winters tend to occur. Similarly, when these indices attain extreme negative values, wet winters tend to occur.

References

Barlow, M., S. Nigam and E. H. Berbery, 2001: ENSO, Pacific decadal variability, and U. S. summertime precipitation, drought, and stream flow. *J. Climate*, **14**, 2105-2128.

Barnston, A. G., and M. Chelliah, 1997: Documentation of a highly ENSO-related SST region in the equatorial Pacific. *Atmos.-Ocean*, **35**, 367-382.

Berri, G. J. and G. Bertossa: Low-level moisture convergence and precipitation anomalies over central South America during the ENSO events of the period 1960-1998. on-line paper.

Bjerknes, J., 1969: Atmospheric teleconnections from the equatorial pacific. *Mon. Wea. Rev.*, **97**, 163-172.

Blumenstock, D. L., and S. Price, 1967: Climates of the United States—Hawaii. U.S. Dept. of Commerce, ESSA, Climatography of the United States, No. 60-51, 27pp. [Available at National Climatic Center, Asheville, NC]

Bond, N. A., and D. E. Harrison, 2000: The Pacific Decadal Oscillation, air-sea interaction and central north Pacific winter atmospheric regimes. *Geophy. Res. Lett.*, **27**, 5, 731-734.

Bove, M. C., 2000: PDO modification of U.S. ENSO climate impacts. MS thesis, Dept. of Meteorology, The Florida State University, 103pp.

Chu, P.S., 1989: Hawaiian drought and Southern Oscillation. *Int. J. Climatol.*, **9**, 619-631.

Chu, P. S., 1995: Hawaii rainfall anomalies and El Niño. *J. Climate*, **8**, 1697-17-3.

Chu, P.S., 2002: Large-scale circulation features associated with decadal variations of tropical cyclone activity over the central North Pacific. *J. Climate*, **15**, 2678-2689.

Chu, P.S., A. J. Nash, and F. Porter, 1993: Diagnostic studies of two contrasting rainfall episodes in Hawaii: Dry 1981 and Wet 1982. *J. Climate*, **6**, 1957-1462.

Hanley, D. E., M. A. Bourassa, J. J. O'Brien, S. R. Smith and E. R. Spade, 2003: A quantitative evaluation of ENSO indices. *J. Climate*, **16**, 1249-1258.

Garbrecht, J.D., and F.E. Rossel: Decadal-scale precipitation increase in the Great Plains at the end of the 20th century.

Gershunov, A., 1998: ENSO Influence on tntreseasonal extreme rainfall and temperature frequencies in the contiguous United States: Implications for long-range predictability. *J. Climate*, **11**, 3192-3203.

Gershunov, A. and T. P. Barnett, 1998: Interdecadal modulation of ENSO teleconnections. *Bull. Amer. Meteor, Soc.*, **79**, 2715-2725.

Gutzler, D. S., D. M. Kann and C. Thornbrugh, 2002: Modulation of ENSO-based long-lead ourlooks of southwestern U.S. winter precipitation by the Pacific Decadal Oscillation. *Wea. and forecast*, **17**, 1163-1172.

Horel, J. D., and J. M. Wallace, 1981: Planetary scale atmospheric phenomena associated with the Southern Oscillation. *Mon. Wea. Rev.*, **109**, 813-829.

Hu, Q., C. M. Woodruff and S. E. Mudrick, 1998: Interdecadal variations of annual precipitation in the central United States. Bull. *Amer. Meteor. Soc.*, **79**, 221-229.

Krishnamurthy, V., and B. N. Goswami, 2000: Indian monsoon-ENSO relationshjp on interdecadal timescale. *J. Climate*, **13**, 579-595.

Lau, K.-M., and H. Weng, 1995: Climate signal detection using wavelet transform: how to make a time series sing. *Bull. Amer. Meteor, Soc.*, **76**, 2391-2402.

Lyons, S. W., 1982: Empirical orthogonal function analysis of Hawaiian rainfall. *J. Appl. Meteor.*, **21**, 1713-1729.

Mantua, N. J., S. R. Hare, Y. Zhang, J. M. Wallace, and R. C. Francis, 1997: A Pacific interdecadal climate oscillation with impacts on salmon production. *Bull. Amer. Meteor. Soc.*, **78**, 1069-1079.

Meisner, B. N., 1976: A study of Hawaiian and Line Islands rainfall. UHMET-76-04, Dept. Meteor., University of Hawaii, 83 pp.

Minboe, S., and N. Mantua, 1999: Interdecadal modulation of interannual atmospheric and oceanic variability over the North Pacific. *Progress in Oceanography*, **43**, 163-192.

Minboe, S., 2000: Spatio-temporal structure of the pentadecadal variability over the North Pacific. *Progress in Oceanography*, **47**, 381-408.

Newman, M., G. P. Compo, and M. A. Alexander, 2003: ENSO-forced variability of the Pacific Decadal Oscillation. *J. Climate* (submitted).

Overland, J.E., J.M. Adams, and H.O. Hofjeld, 2000: Chaos in the north Pacific: spatial modes and temporal irregularity. *Progress in Oceanography*, **47**, 337-354.

Pierce, D. M., 2002: The role of sea surface temperatures in interactions between ENSO and the north Pacific oscillation. *J. Climate*, **15**, 1295-1308.

Paegle, J. N. and K. C. Mo, 2002: Linkages between summer rainfall variability over

South America and sea surface temperature anomalies. *J. Climate*, **15**, 1389-1407.

Papineau, J. M., 2001: Wintertime temperature anomalies in Alaska correlated with ENSO and PDO. *Int. J. Climatol.*, **21**, 1577-1592.

Ropelewski, C. F., and M. S. Halpert, 1987: Global and regional scale precipitation patterns associated with the El Niño/Southern Oscillation. *Mon. Wea. Rev.*, **115**, 1606-1626.

Schroeder, T. A., 1997: Meteorological analysis of an Oahu flood. *Mon. Wea. Rev.*, **105**, 458-468.

Taylor, G. E., 1984: Hawaiian winter rainfall and its relation to the Southern Oscillation. *Mon. Wea. Rev.*, **112**, 1613-1619.

Torrence, C., and G. P. Compo, 1998: A practical guide to wavelet analysis. *Bull. Amer. Meteor. Soc.*, **79**, 61-78.

Trenbeth, K. E., and J. W. Hurrel, 1994: Decadal atmosphere-ocean variations in the Pacific. *Climate Dyn.*, **9**, 303-319.

Trenbeth, K. E., 1997. The definition of El Niño. *Bull. Amer. Meteor. Soc.*, **78**, 2771-2777.

Wallace, J. M., and D. S. Gutzler, 1981: Teleconnections in the geopotential height field during the Northern Hemisphere winter. *Mon. Wea. Rev.*, **109**, 784-812.

Horel, J. D., and J. M. Wallace, 1981: Planetary-scale atmospheric phenomena associated with the Souther Oscillation. *Mon. Wea. Rev.*, **109**, 813-829.

Walker, G.T., and E.W. Bliss, 1932: World Weather *V. Men. Roy. Meteor. Soc.*, **4**, 119-139.

Wang, B., and Y. Wang, 1996: Temporal structure of the southern oscillation as revealed by waveform and wavelet analysis. *J. Climate*, **9**, 1586-1598.

Weng, H., and K.-M. Lau, 1994: Wavelet, period doubling, and time-freqency localization with application to organization of convection over the tropical western pacific. *J. Atmos. Sec.*, **51**, 2523-41.

Yeh, T. C., C. C. Wallen, and J. E. Carson, 1951: A study of rainfall over Oahu. Meteorol. Monogr., *Amer. Meteor. Soc.*, **3**, 34-46.

Zhang, Y., J. M. Wallace, and D. S. Battisti, 1997: ENSO-like Interdecadal Variability: 1900-93. *J. Climate*, **10**, 1004-1020.

Table 1. List of rainfall stations used for HRI. Stations on each island are arranged so that the first three stations are windward, the next three are neutral, and the last three are leeward. For each side of the island, the station is arranged from high to low elevation. Solidus denotes replacement station follow. Asterisk denotes new stations.

Station	Code number	Lat (N) /Long (W)	Elevation (m)	Record length
Kauai				
1. Iliilula Intake /	1050.00	22 02 34/159 28 18	326.2	1935-1986
North Wailua Ditch*	1051.00	22 03 57/159 28 12	338.4	1987-2000
2. Koloa Mauka	994.00	21 57 50/159 26 36	195.1	1905-2002
3. Kealia /	1112.00	22 06 10/159 18 30	3.0	1905-1986
Anahola*	1114.00	22 08 15/159 18 24	54.9	1987-2000
4. Wahiawa Mt./	990.00	21 58 30/159 30 35	655.4	1905-1972
Alexander Reservoir*	983.00	21 57 34/159 31 43	423.6	1973-2002
5. East Lawai	934.00	21 54 30/159 29 48	134.1	1905-2002
6. Kukuiula	935.00	21 53 30/159 29 30	32.0	1905-2002
7. Puehu Ridge	1040.00	22 01 07/159 41 42	506.1	1940-2000
8.Brydeswood Station	985.00	21 55 42/159 32 12	219.5	1910-2002
9. Waiawa	943.00	21 58 50/159 43 58	3.0	1905-1999
Oahu				
10. Nuuanu Res.	783.00	21 21 21/157 48 37	320.1	1905-2002
11. Waikane /	885.00	21 30 12/157 53 24	243.9	1917-1982
Waiahola*	837.00	21 28 24/157 52 58	227.1	1983-2002
12. Kahuku	912.00	21 40 48/157 57 12	7.6	1905-2002
13. Wahiawa Dam	863.00	21 30 00/158 03 08	260.6	1905-1999
14. Waimea	892.00	21 37 43/158 04 03	128.0	1917-2002
15. Waialua	847.00	21 34 36/158 07 24	4.5	1905-2000
16. Waianae Mauka/	803.00	21 29 25/158 08 04	480.1	1905-1973
Hokuloa*	725.20	21 24 36/158 05 48	594.7	1974-1999
17.Aiea Field/	761.00	21 24 30/157 56 36	138.7	1908-1969
Aiea*	764.50	21 24 26/157 54 35	213.4	1970-2002
18. Ewa Mill	741.00	21 20 38/158 02 12	22.8	1905-2002
Hawaii				
19. Hakalau Mauka/	135.00	19 53 12/155 10 06	350.6	1906-1978
Honomu Mauka*	138.00	19 51 06/155 08 48	382.8	1979-2002
20. Paauhau	217.00	20 05 12/155 26 24	121.9	1905-1999
21. Papaiku Makai	144.10	19 47 12/155 26 24	60.9	1905-2002
22. Kiolakaa	6.00	19 04 24/155 38 18	586.8	1929-1998
23. Naalehu	14.00	19 03 48/155 38 18	205.7	1905-2002
24. Kapolo /	93.00	19 30 48/155 35 24	33.5	1905-1959
Hayhalalekai*	67.50	19 28 30/154 50 06	4.6	1960-2002
25. Kaawaloa	29.00	19 29 42/155 55 12	408.5	1942-1999
26. Napoopoo	28.00	19 28 18/155 58 30	121.9	1940-2002
27. Halualoa Beach/	68.00	19 36 30/155 58 47	53.0	1919-1978
Kainaliu Beach*	73.12	19 31 54/155 57 24	5.2	1979-1998

Table 2. Listings of winter and summer El Niño and La Niña events since 1951. The mean and median precipitation (unit: inch) for each subset is indicated.

Winter:

	# of yrs		Mean	Median
Climatology	49	1951~1999	35.0873	28.0900
El Niño	12	1952,1966,1969,1970,1973, 1977,1980,1983,1987,1992, 1995,1998	30.1499	21.3250
El Niño/+PDO	7	1977,1980,1983,1987,1992, 1995,1998	24.6383	17.5500
El Niño/-PDO	5	1952,1966,1969,1970,1973	37.7723	28.4800
La Niña	11	1951,1955,1956,1971,1974, 1975,1976, 1985,1989,1996, 1999	42.0487	34.9050
La Niña/+PDO	4	1985,1989,1996,1999	36.6072	29.5800
La Niña/-PDO	7	1951,1955,1956,1971,1974, 1975,1976	45.1558	37.5350

Summer:

	# of yrs		Mean	Median
Climatology	49	1951~1999	21.9516	14.8000
El Niño	10	1953,1957,1965,1969,1972, 1982,1987,1991,1993,1997	23.7536	18.7103
El Niño/+PDO	5	1982,1987,1991,1993,1997	26.5266	17.6224
El Niño/-PDO	5	1953,1957,1965,1969,1972	21.0039	19.1427
La Niña	7	1955,1956,1964,1971,1975, 1988,1999	16.2700	11.7500
La Niña/+PDO	2	1988,1999	17.5000*	11.7000*
La Niña/-PDO	5	1955,1956,1964,1971,1975	14.2800*	11.7500*

** The summer La Niña/+PDO is not preventative because of the small sample size.

40

Table 3. Correlation coefficients between various 11-year running mean indices for the period 1906-2001.

	HRI	PDO	NPI
HRI	1.0		
PDOI	-0.485	1.0	
NPI	0.652	-0.608	1.0
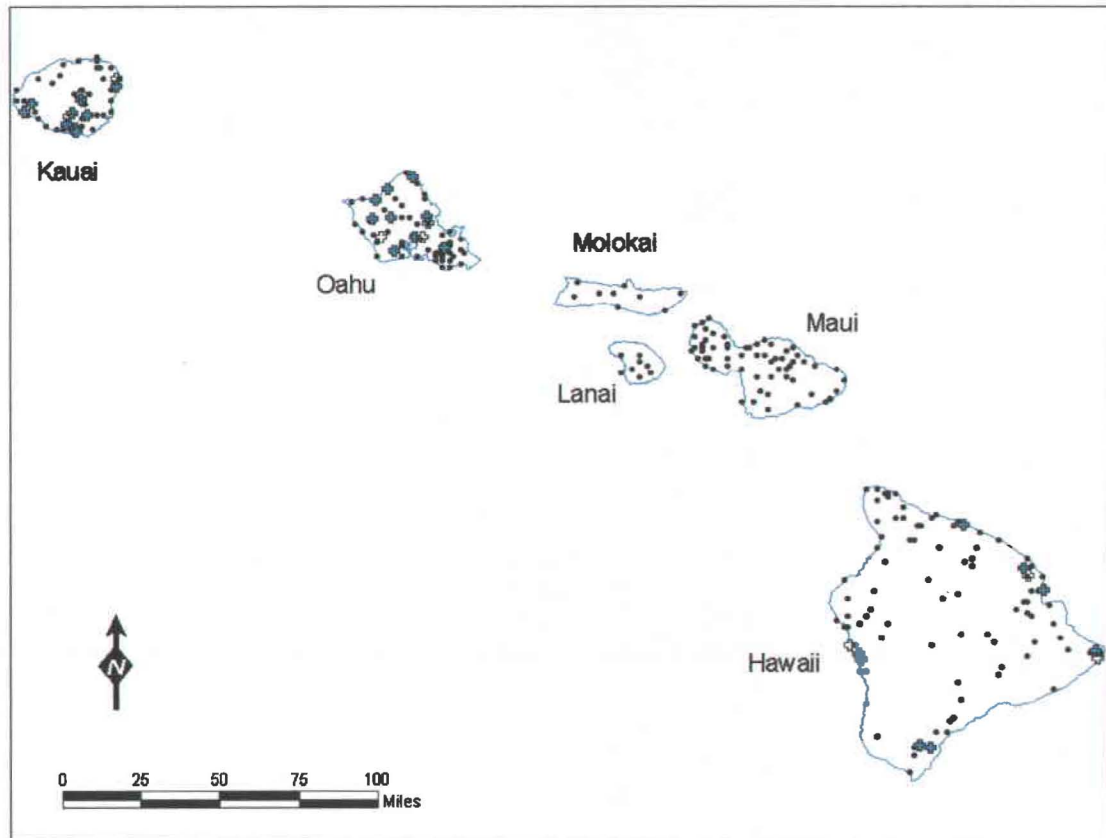
Fig. 1. Map of the major Hawaiian Islands and the location of rainfall stations used in this study. Closed crosses indicate stations used for HRI, and open crosses indicate new stations used to replace the old ones nearby.
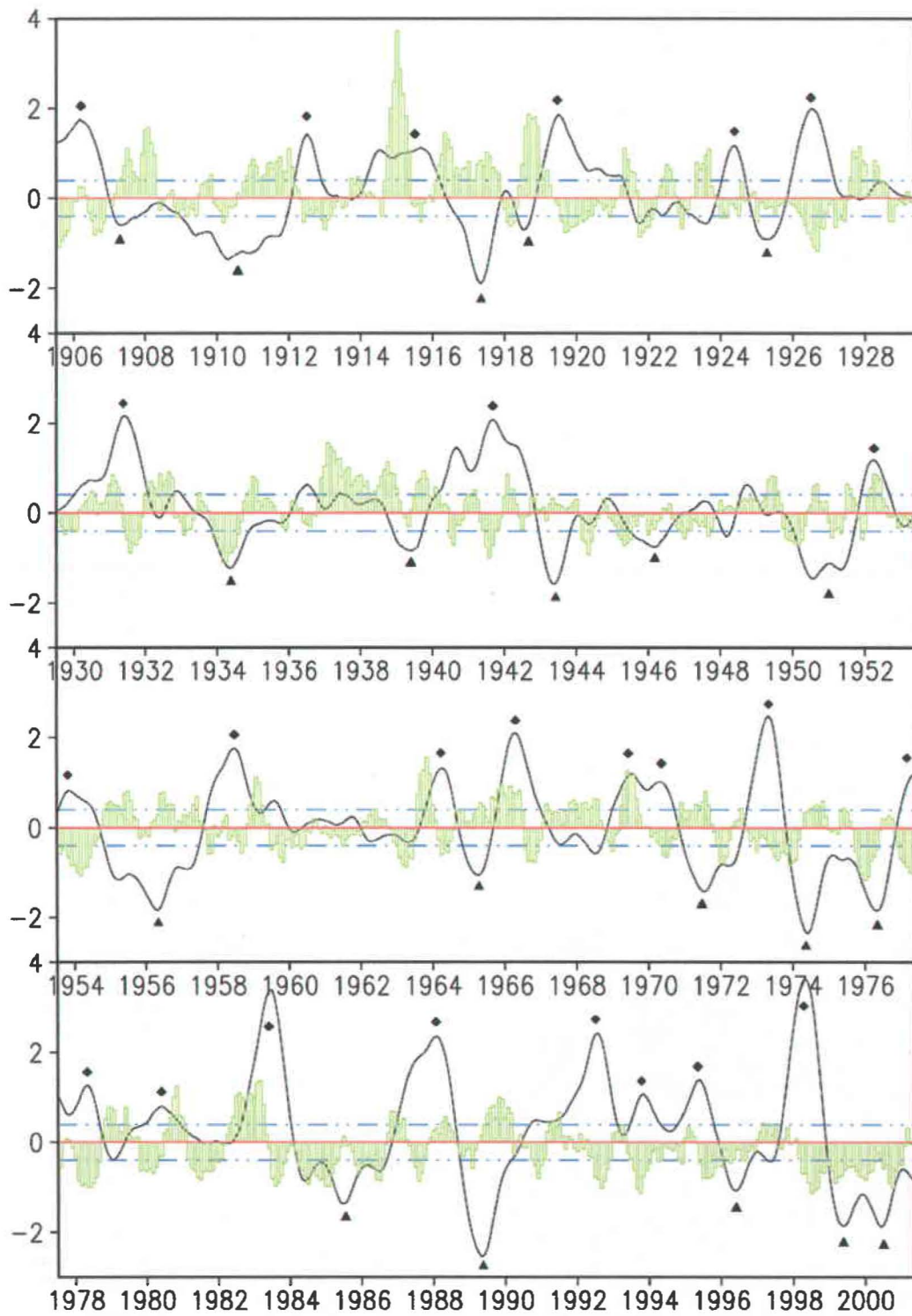
Fig. 2. Time series of 5-month running mean of Niño 3.4 (line) and HRI (bar). The dashed lines are thresholds of ±0.4°C. Diamonds indicate El Niño events, triangles indicate La Niña events.
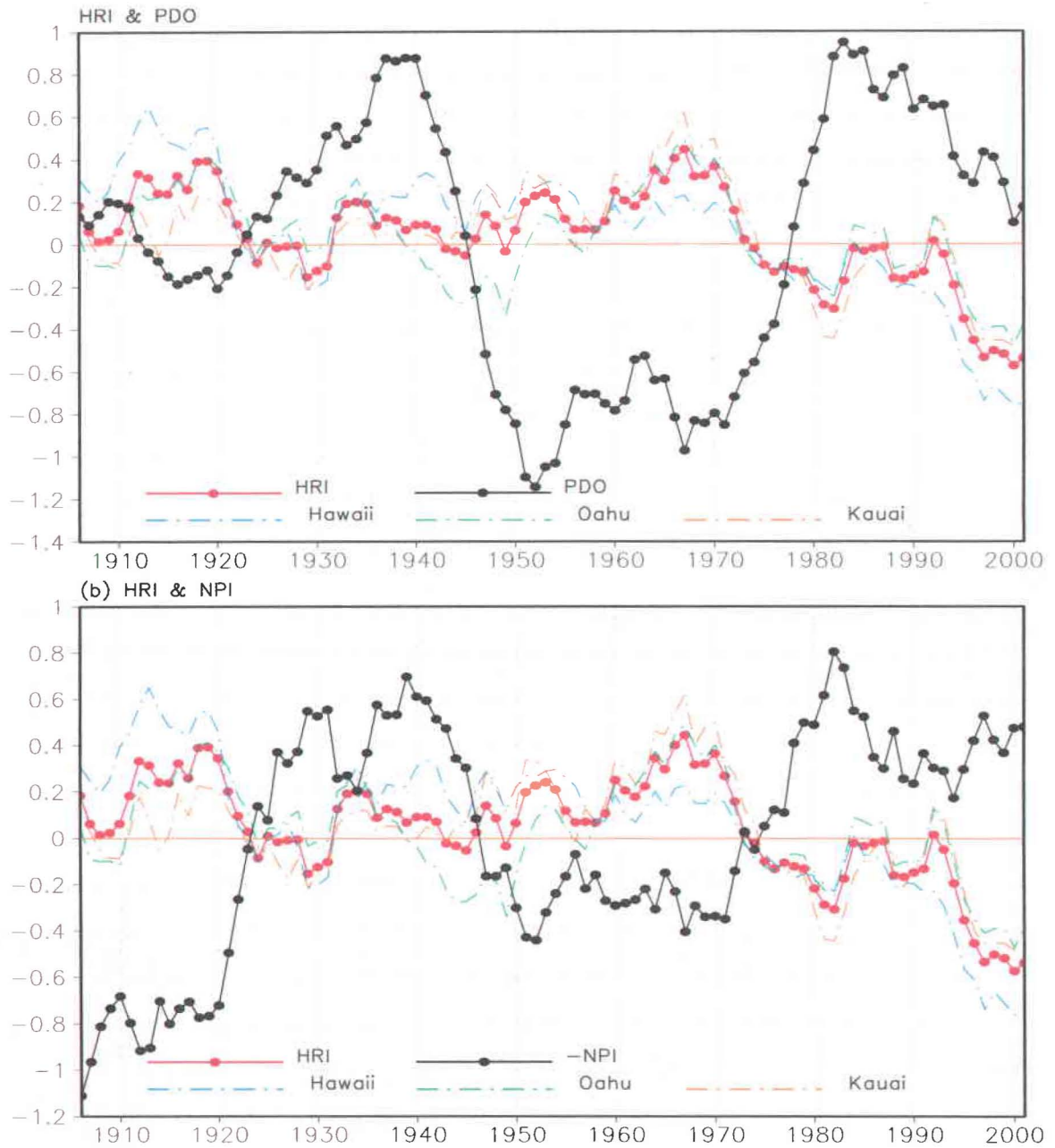
Fig. 3. (a) Time series of 11-year running mean for the PDOI (black dotted), HRI (red dotted) and the annual rainfall for individual islands: Hawaii (blue dash), Oahu (green dash), and Kauai (orange dash). (b) Same as (a) except for reversed NPI (-NPI, red dotted).

44
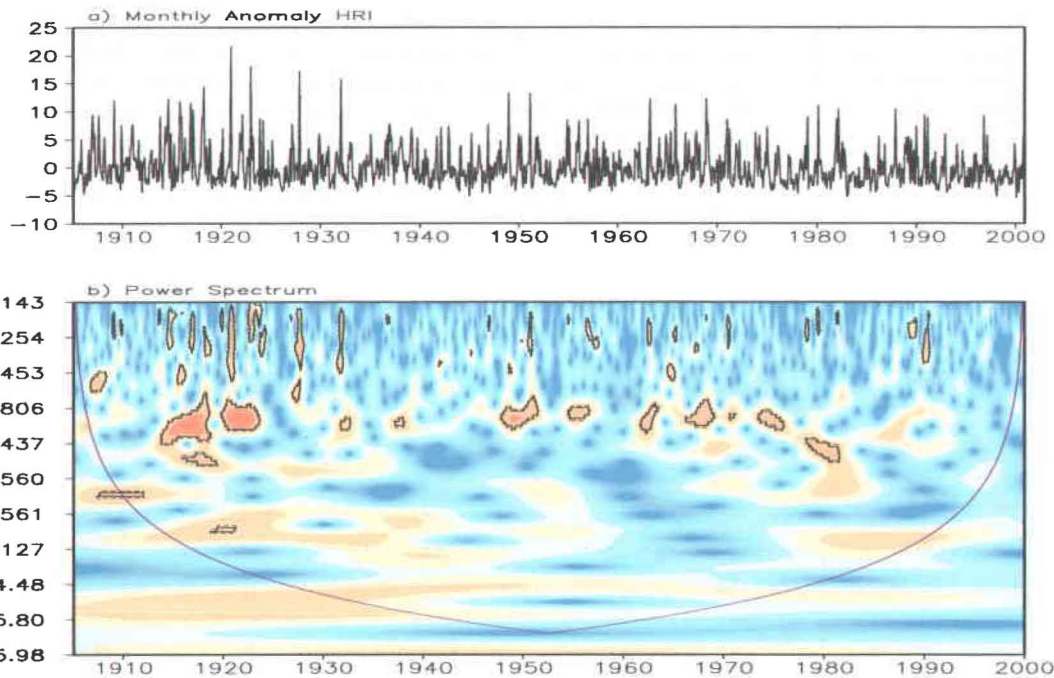
Fig. 4. a) Time series of monthly anomalous HRI. (b) Power spectrum of wavelet analysis and shadings represent different energy density with high amplitude in orange and low amplitude in blue. Black contours enclose regions of greater than 95% confidence for a red-noise process with a lag-1 coefficient of 0.287. The region from the purple curve to the bottom of the figure indicates the "cone of influence". The Y-coordinate is wavelet scale in years.
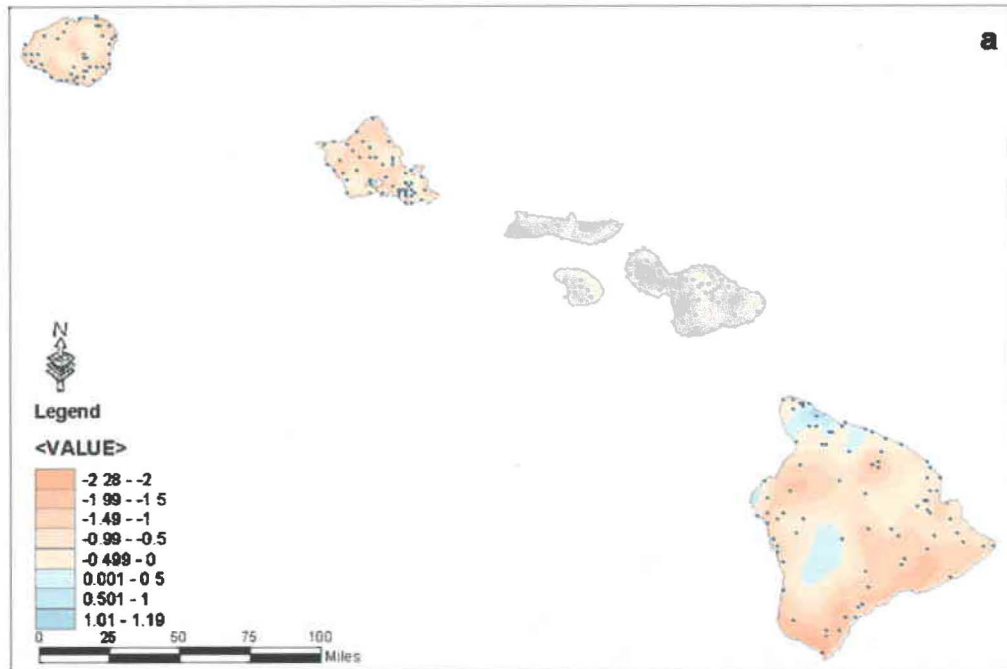
Fig. 5. Winter precipitation difference of a) El Niño minus La Niña, b) positive PDO minus negative PDO.
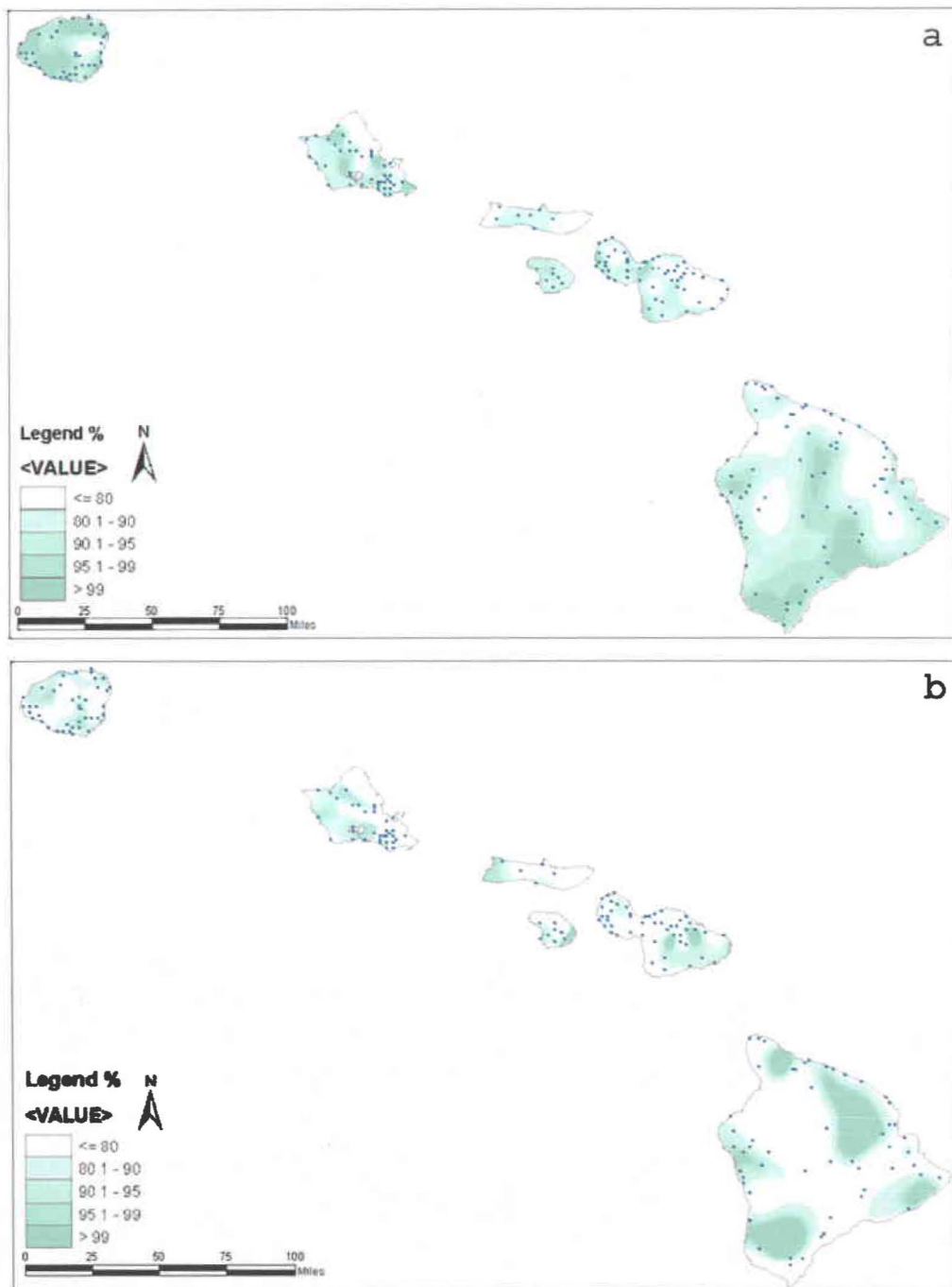
Fig. 6. The nonparametric Mann-Whitney test for the winter precipitation difference of a) El Niño minus La Niña, b) positive PDO minus negative PDO.
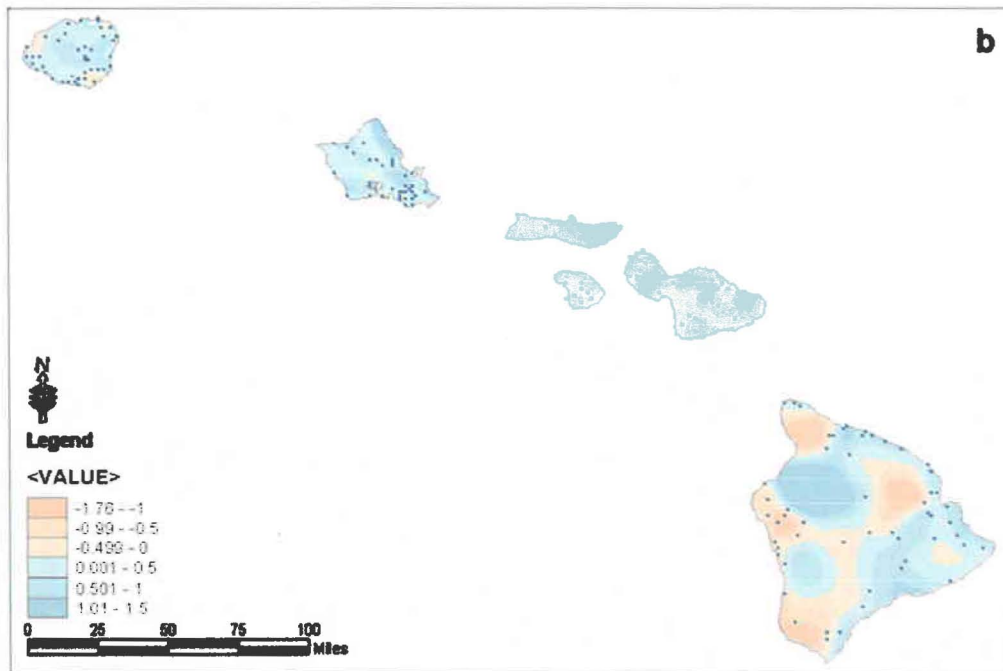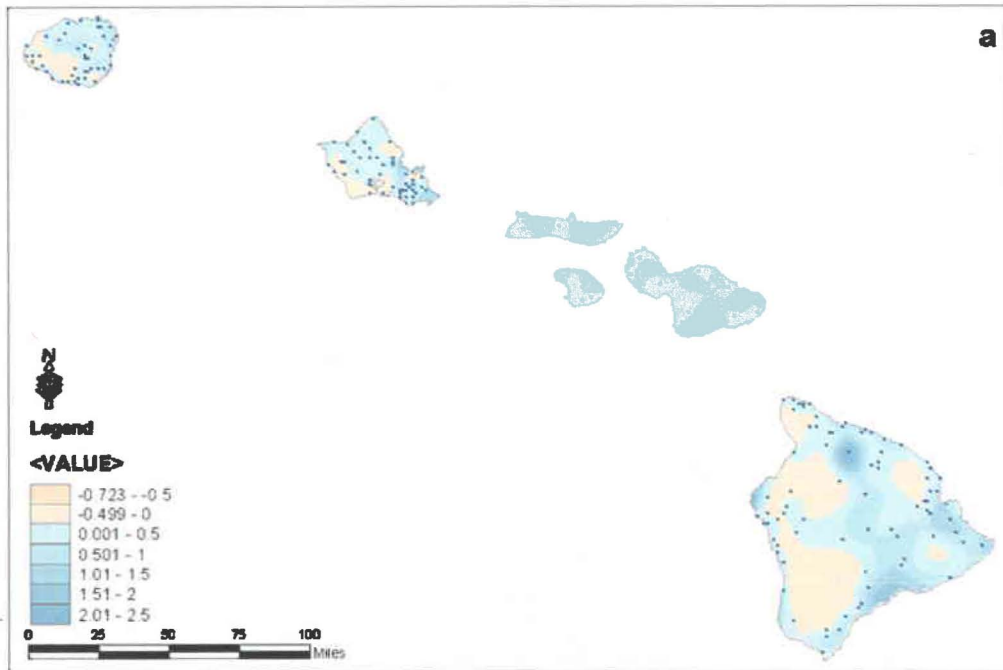
Fig. 7. Summer precipitation difference of a) El Niño minus La Niña, b) positive PDO minus negative PDO.
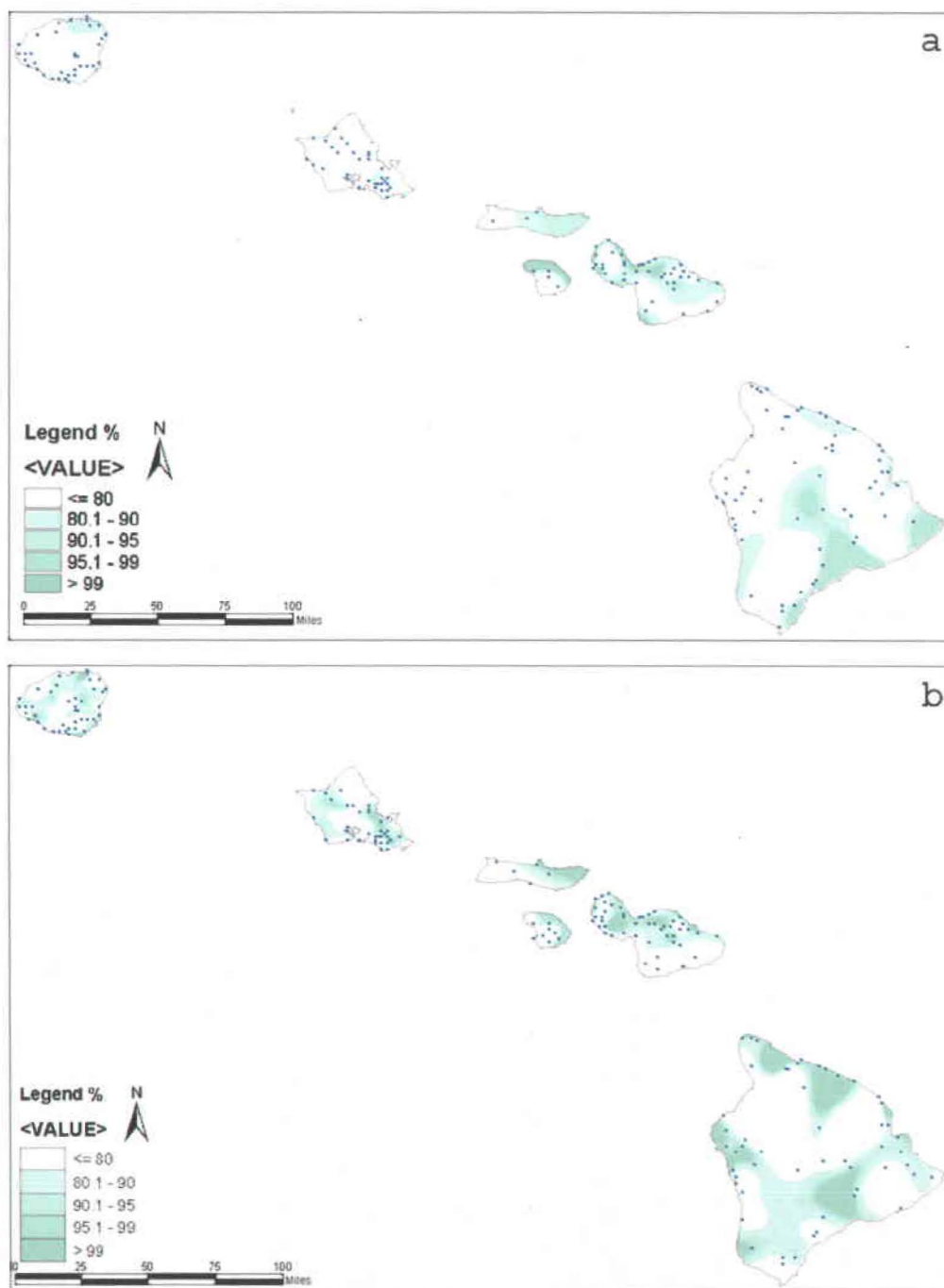
Fig. 8. The nonparametric Mann-Whitney test for the summer precipitation difference of
a) El Niño minus La Niña, b) positive PDO minus negative PDO.

a)200mb wind El Nino—La Nina (NDJFM)

b)200mb wind (+PDO)—(−PDO) (NDJFM)
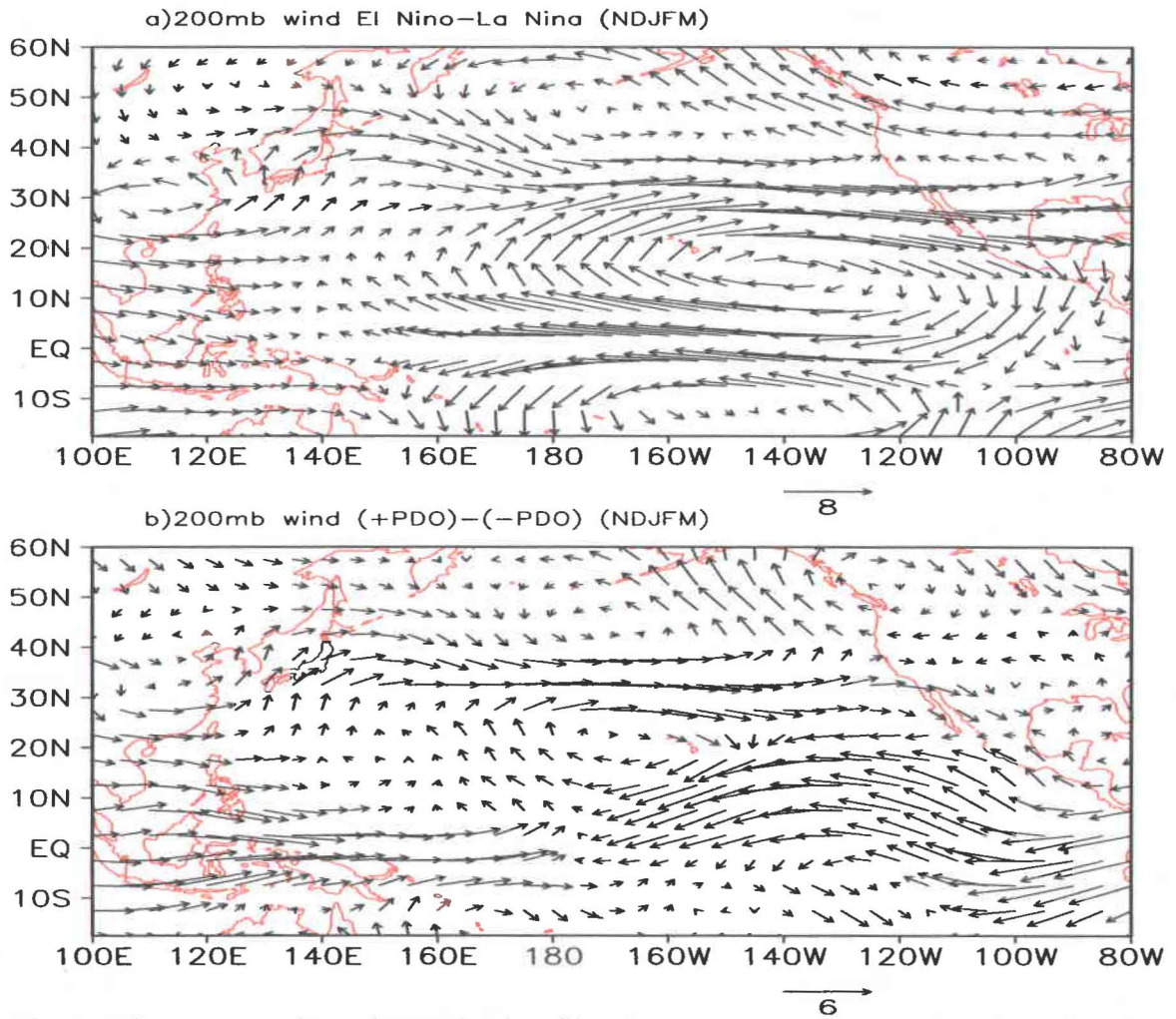
Fig. 9. Winter composites of 200mb wind filed (vectors): (a) El Niño minus La Niña , (b) positive PDO minus negative PDO. The unit for the wind vectors is m/s.
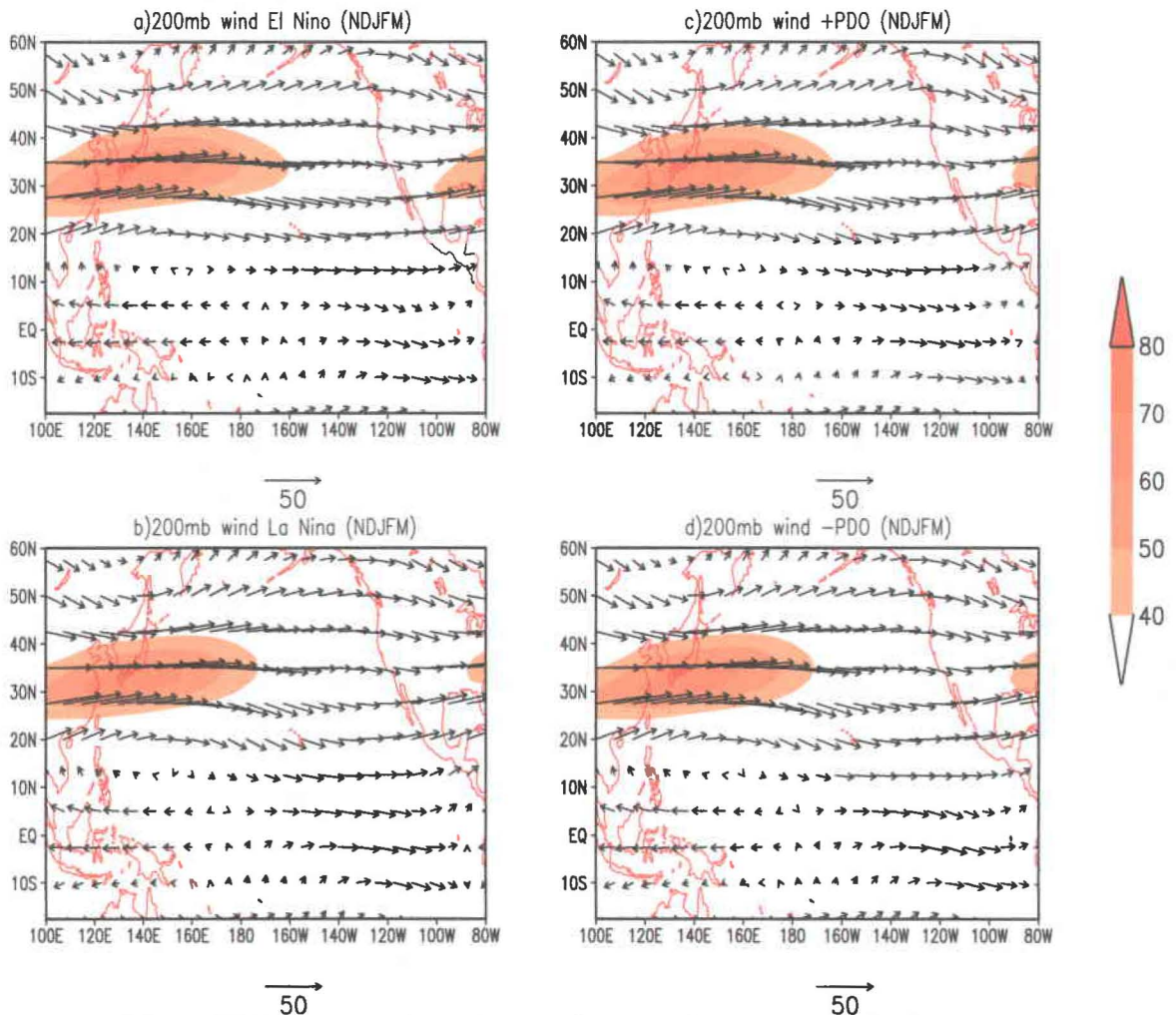
Fig. 10. Winter 200mb wind filed (vectors) for: (a) El Niño, (b) La Niña, (c) positive PDO, and (d) negative PDO. Area with wind speed greater than 40 m/s is shaded.
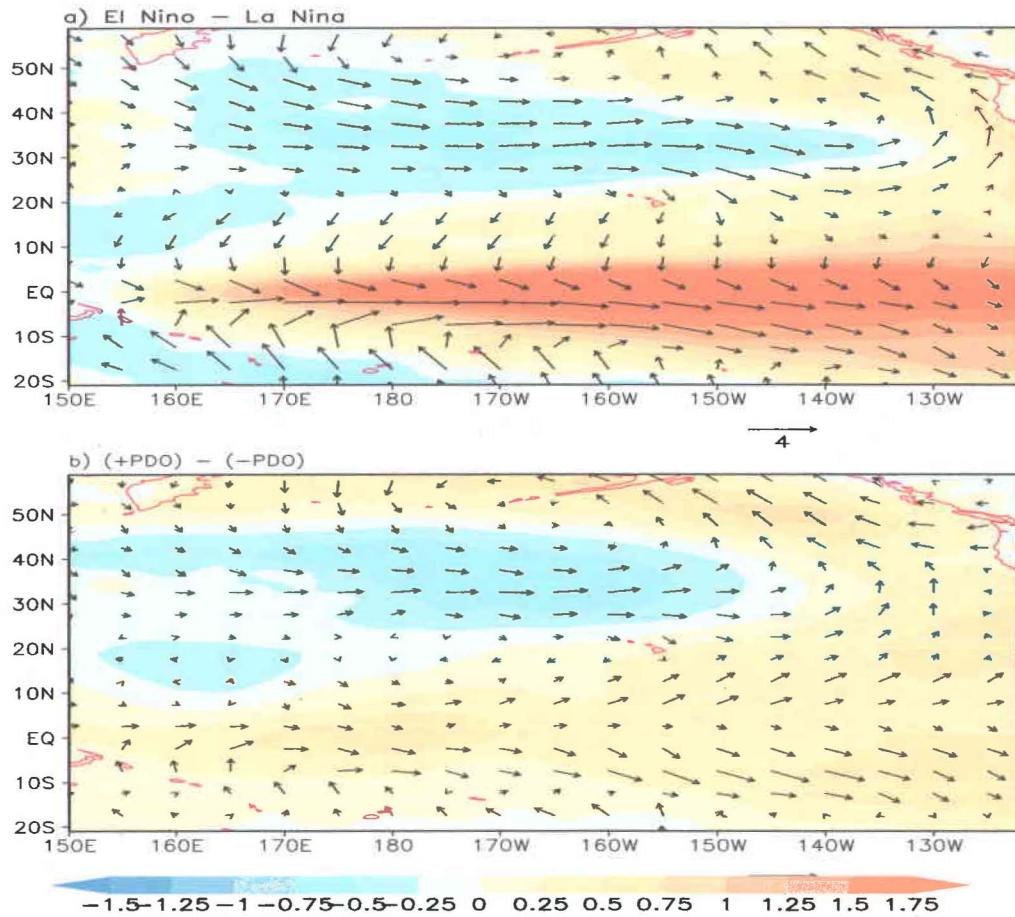
Fig. 11. Winter composites of sea surface temperature (shading) and surface wind (vectors): (a) El Niño minus La Niña, (b) positive PDO minus negative PDO. The unit for SST is °C, while the unit for the wind vectors is m/s.
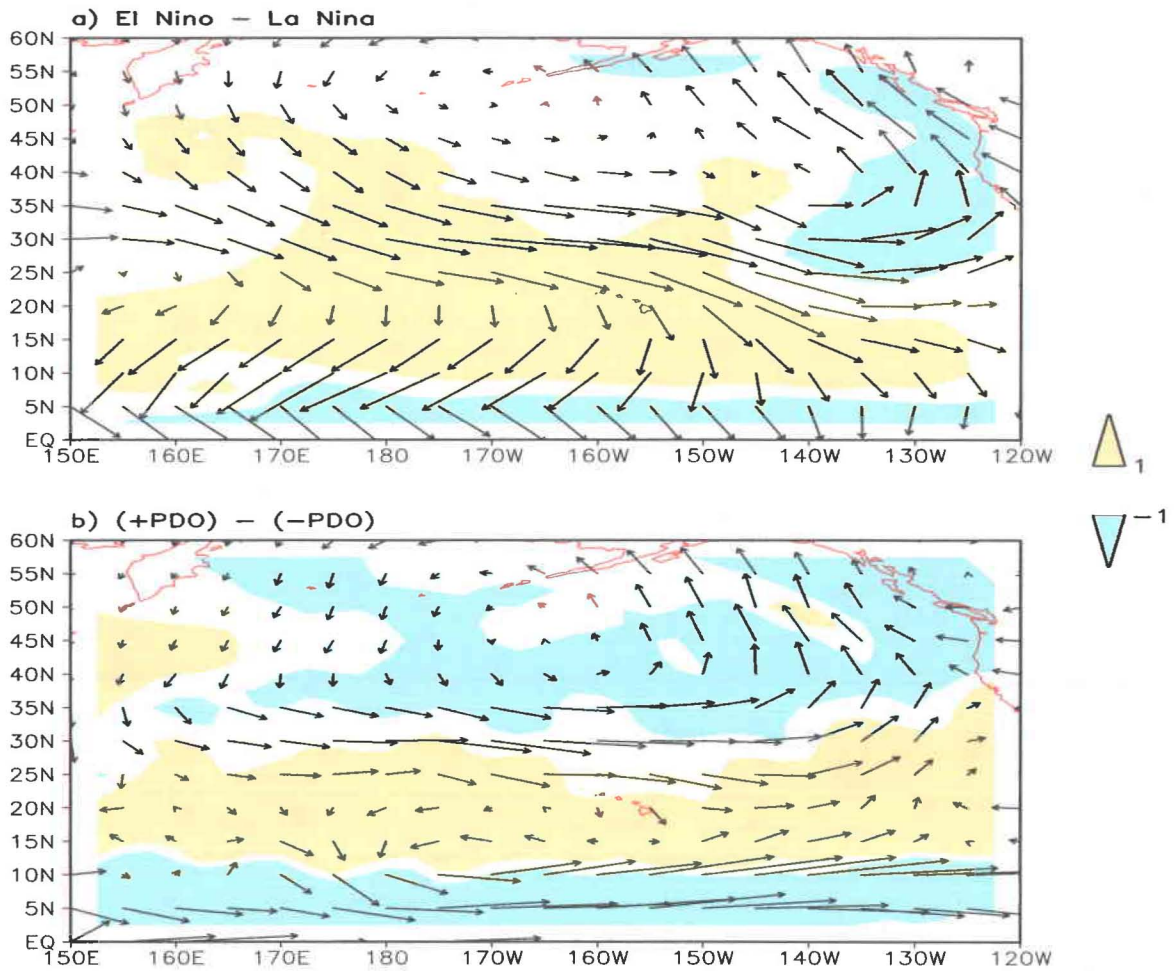
Fig. 12. Winter composites of vertically integrated moisture flux (qu,qv) (vectors) and moisture flux divergence D(Q) (shading): (a) El Niño minus La Niña, (b) positive PDO minus negative PDO. Values for D(Q) greater (less) than 1(-1) mm day^{-1} are shaded yellow (blue). The unit for flux is g (cm s)$^{-1}$.
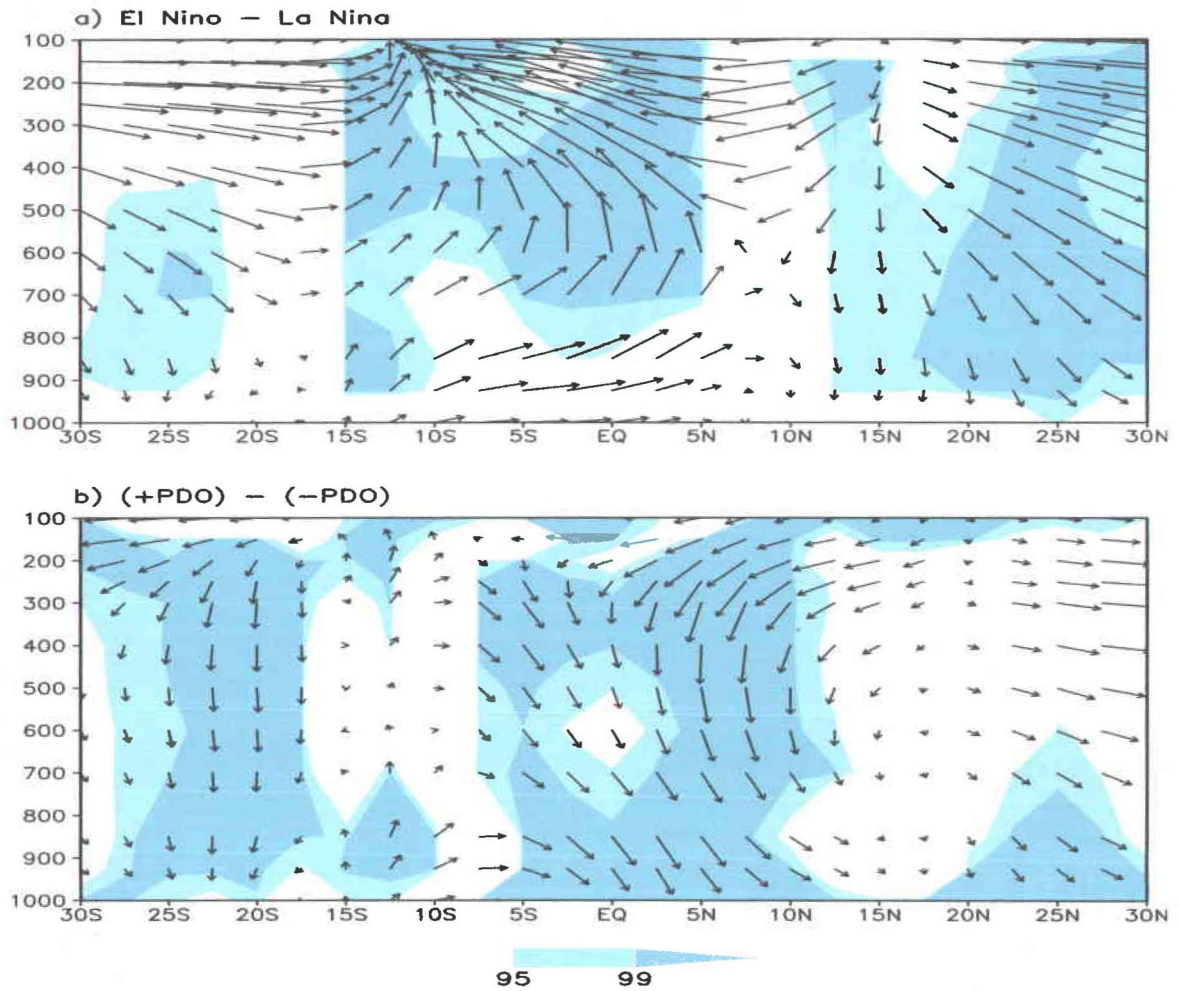
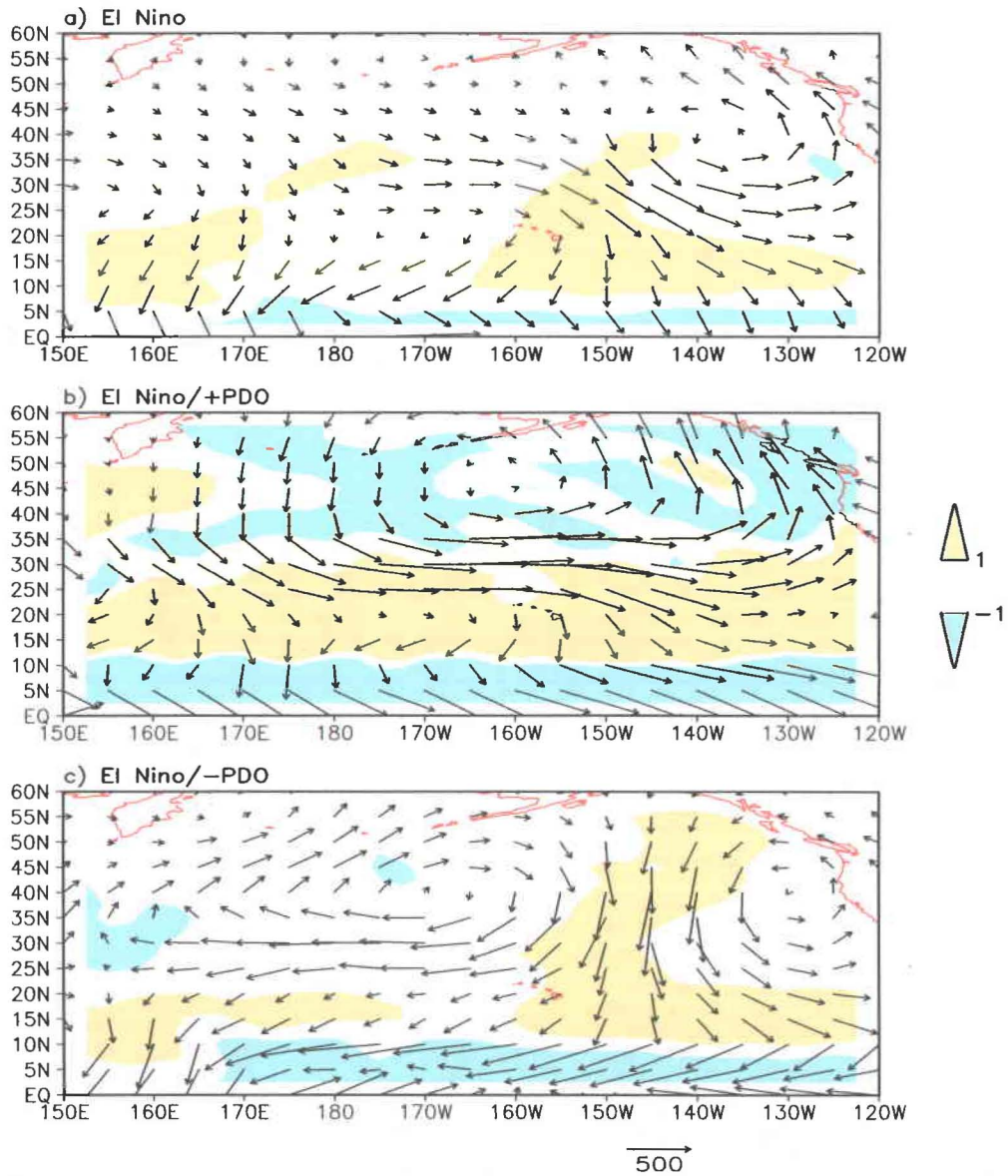Fig. 13. Winter composites of north-south vertical circulation: (a) El Niño minus La Niña, (b) positive PDO minus negative PDO. The latitude-height section of meridional wind and negative pressure vertical velocity (V,-ω) is averaged over 165°W-150°W. Shading is nonparametric Mann-Whitney test based on the vertical velocity at the 95% and 99% levels. The unit vector in the horizontal direction is 6 m/s while that in the vertical direction is 0.03 Pa/s.
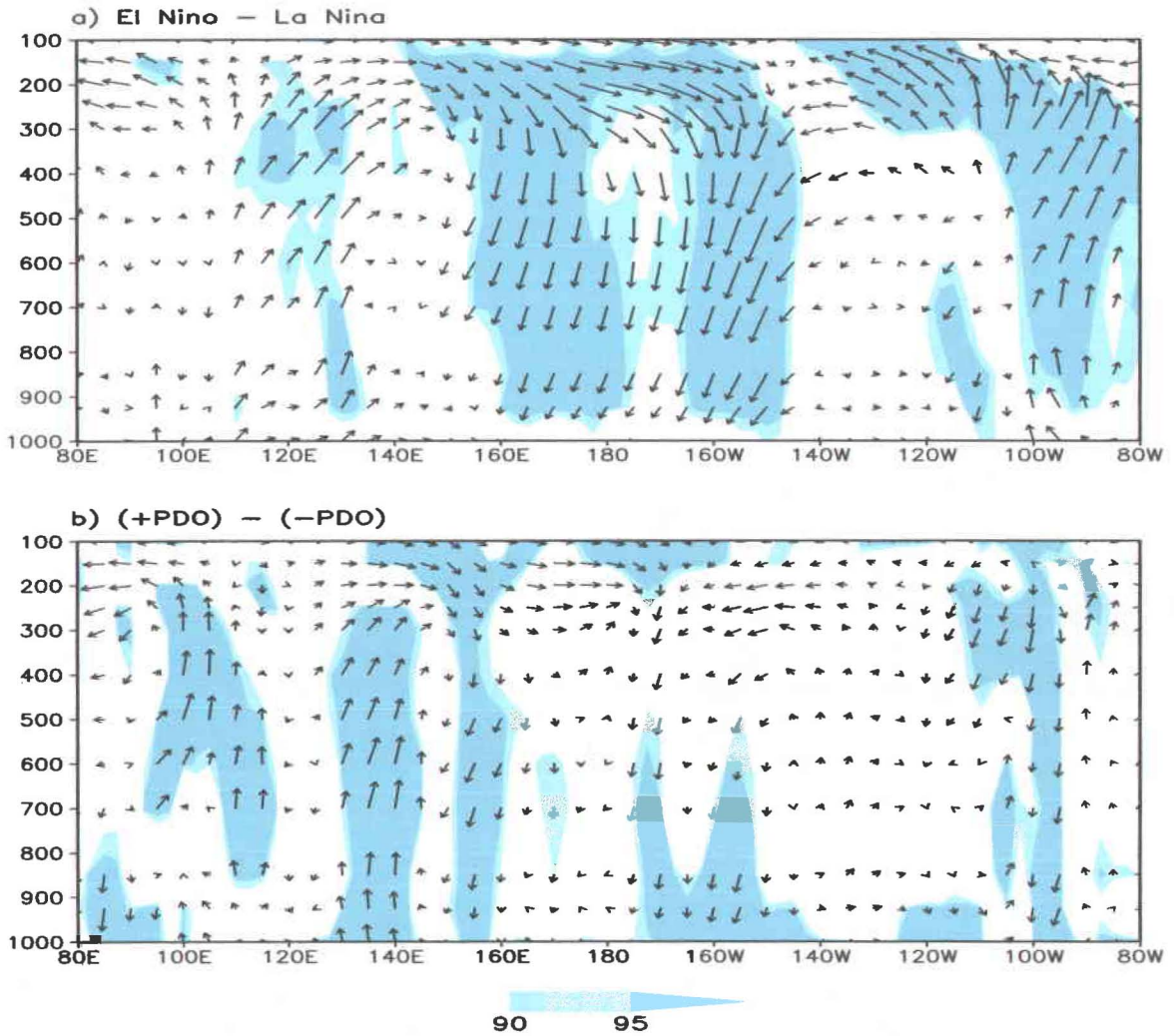
Fig. 14. Winter composites of east-west vertical circulation: (a) El Niño minus La Niña, (b) positive PDO minus negative PDO. Longitude-height section of zonal wind and negative pressure vertical velocity (U,-ω) is averaged over 15°N-25°N. Shading is nonparametric Mann-Whitney test based on the vertical velocity at the 95% and 99% levels. The unit vector in the horizontal direction is 6 m/s, while that in the vertical direction is 0.03 Pa/s.
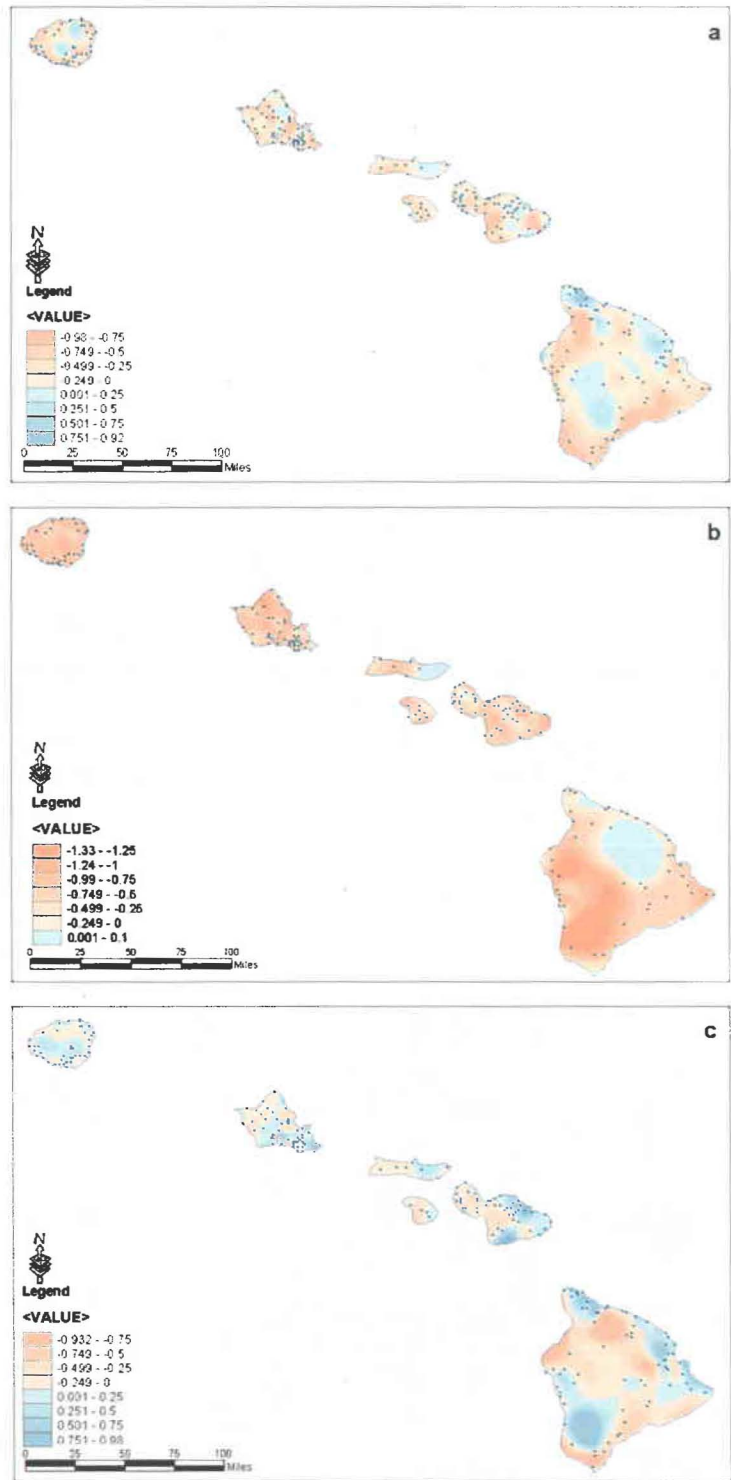
Fig. 15. Winter precipitation anomalies for: a) El Niño, b) El Niño/+PDO, and c) El Niño/-PDO.
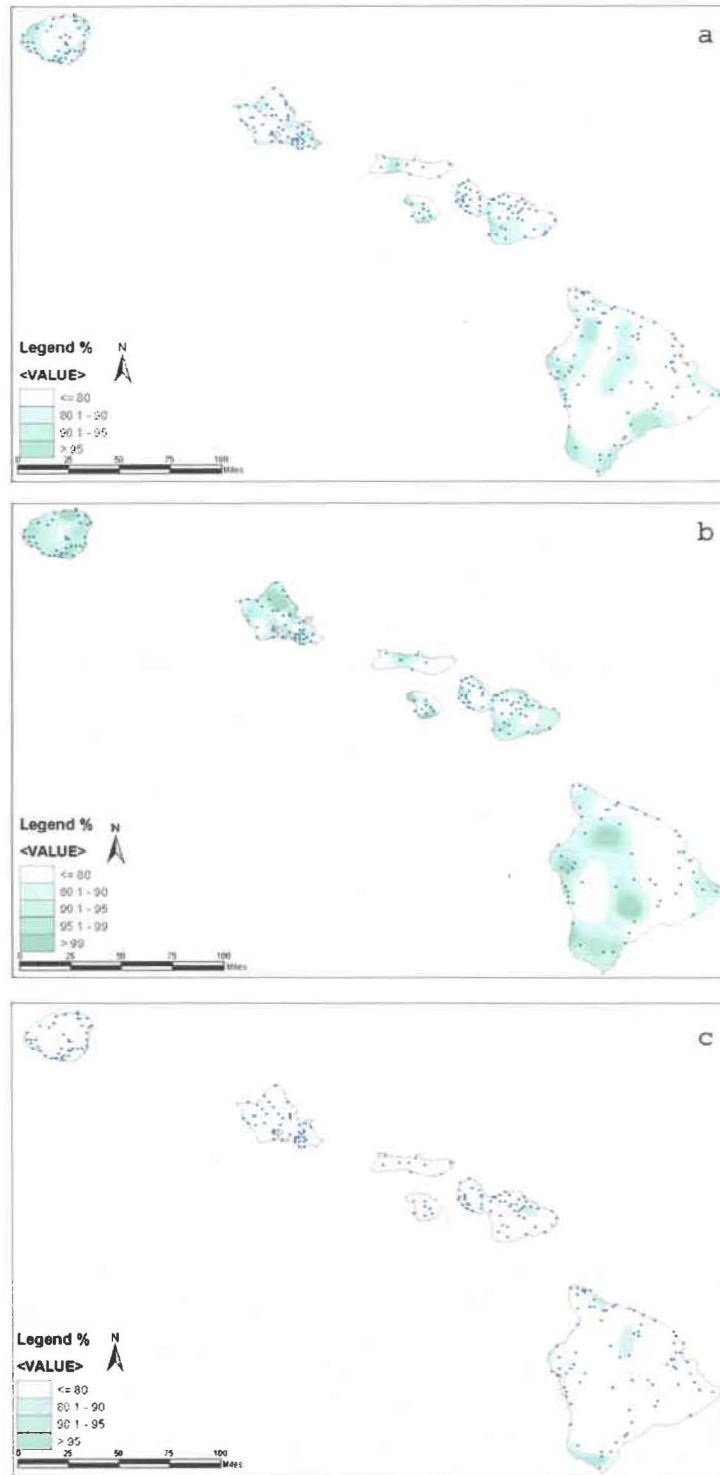
Fig. 16. The nonparametric Mann-Whitney test of winter precipitation anomalies for: a) El Niño, b) El Niño/+PDO, and c) El Niño/-PDO.
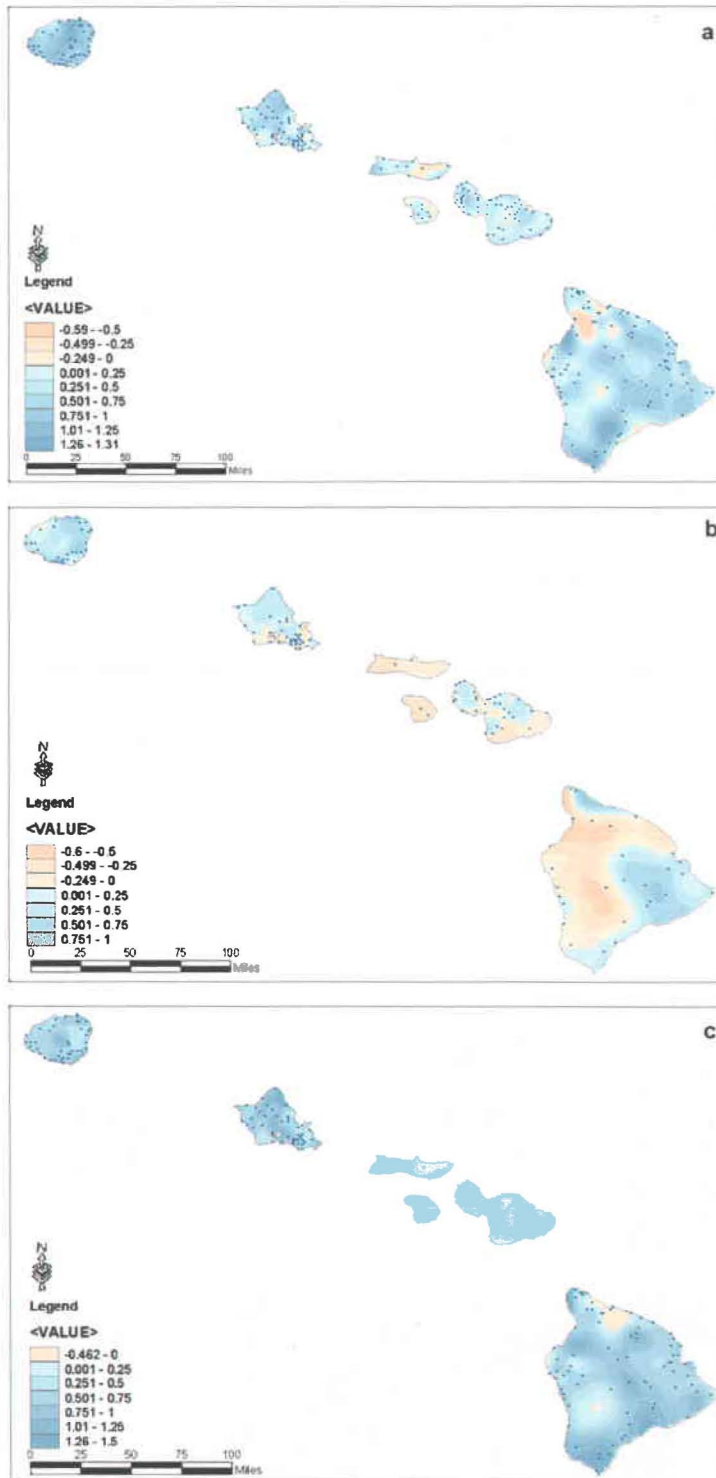
Fig. 17. Winter precipitation anomalies for: a) La Niña, b) La Niña/+PDO, and c) La Niña/-PDO.
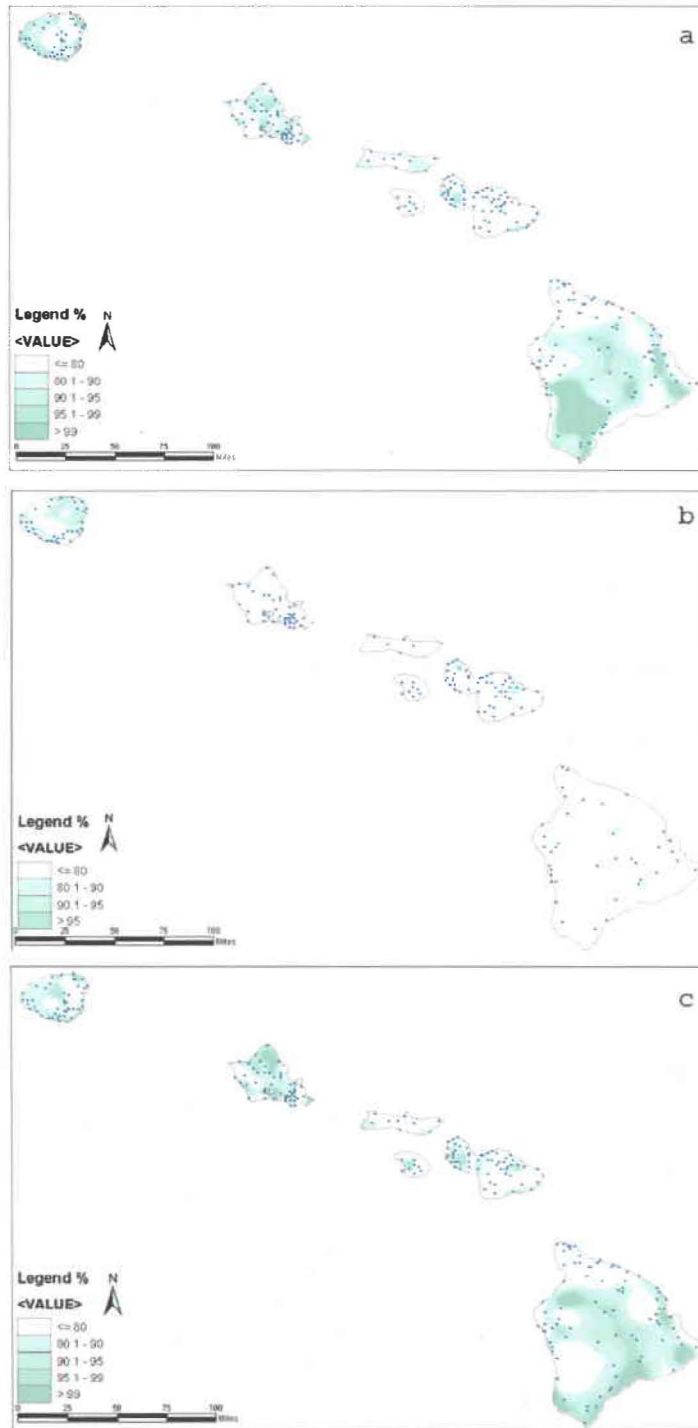
Fig. 18. The nonparametric Mann-Whitney test of winter precipitation anomalies for: a) La Niña , b) La Niña/+PDO, and c) La Niña/-PDO.
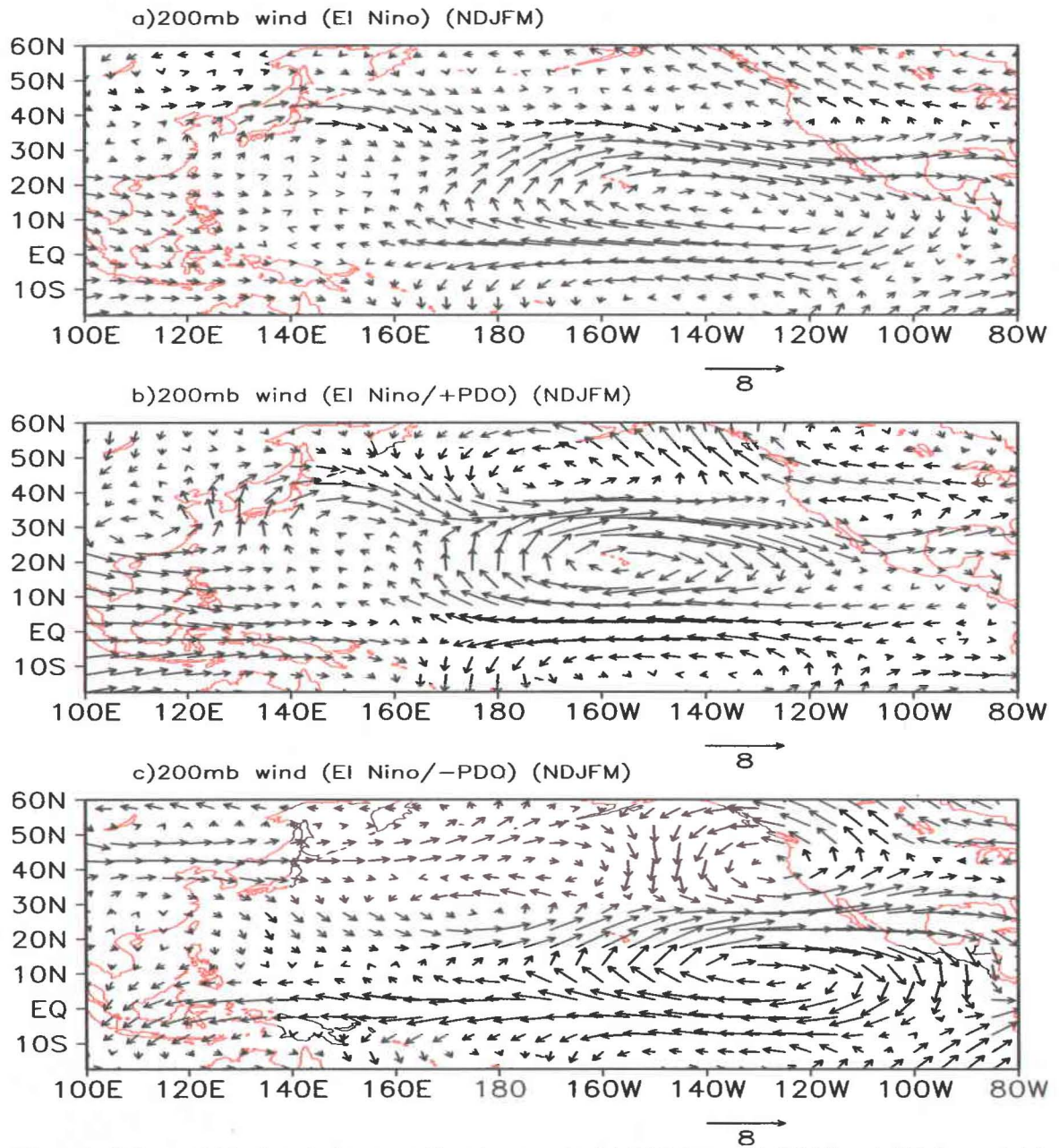
Fig. 19. Winter 200mb wind anomalies (vectors): (a) El Niño, (b) El Niño/+PDO, and (c) El Niño/-PDO. The unit for the wind vectors is m/s.
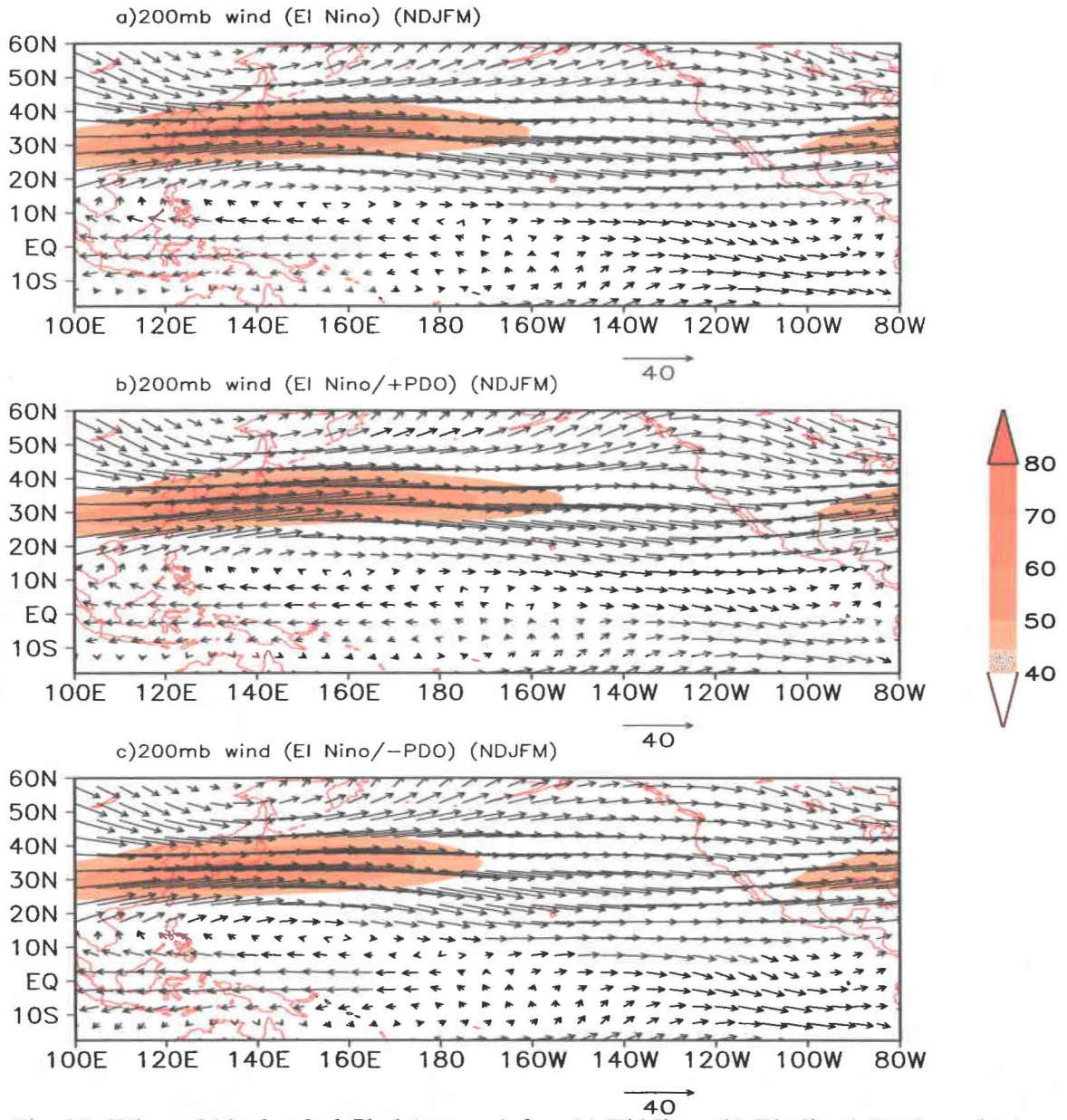
Fig. 20. Winter 200mb wind filed (vectors) for: (a) El Niño, (b) El Niño/+PDO, and (c) El Niño/-PDO. Area with wind speed greater than 40 m/s is shaded.
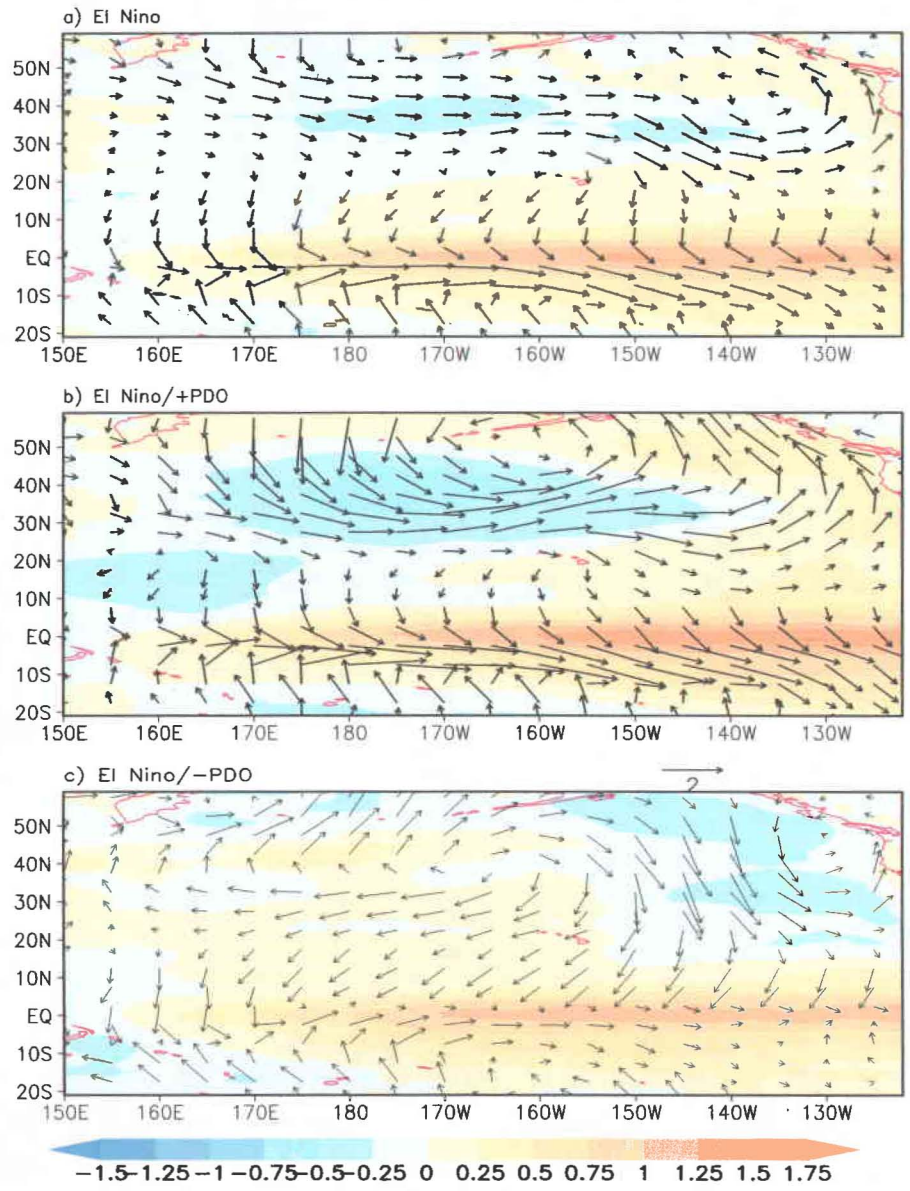
Fig. 21. Winter sea surface temperature (shading) and surface wind (vectors) anomalies: (a) El Niño, (b) El Niño+ PDO, and (c) El Niño/-PDO. The unit for SST is °C, while the unit for the wind vectors is m/s.

Fig. 22. Winter vertically integrated moisture flux (qu,qv) (vectors) and moisture flux divergence D(Q) (shading) anomalies: (a) El Niño, (b) El Niño/+ PDO, and (c) El Niño/-PDO. Values for D(Q) greater (less) than 1(-1) mm day^{-1} are shaded yellow (blue). The unit for flux is g (cm s)$^{-1}$.

63
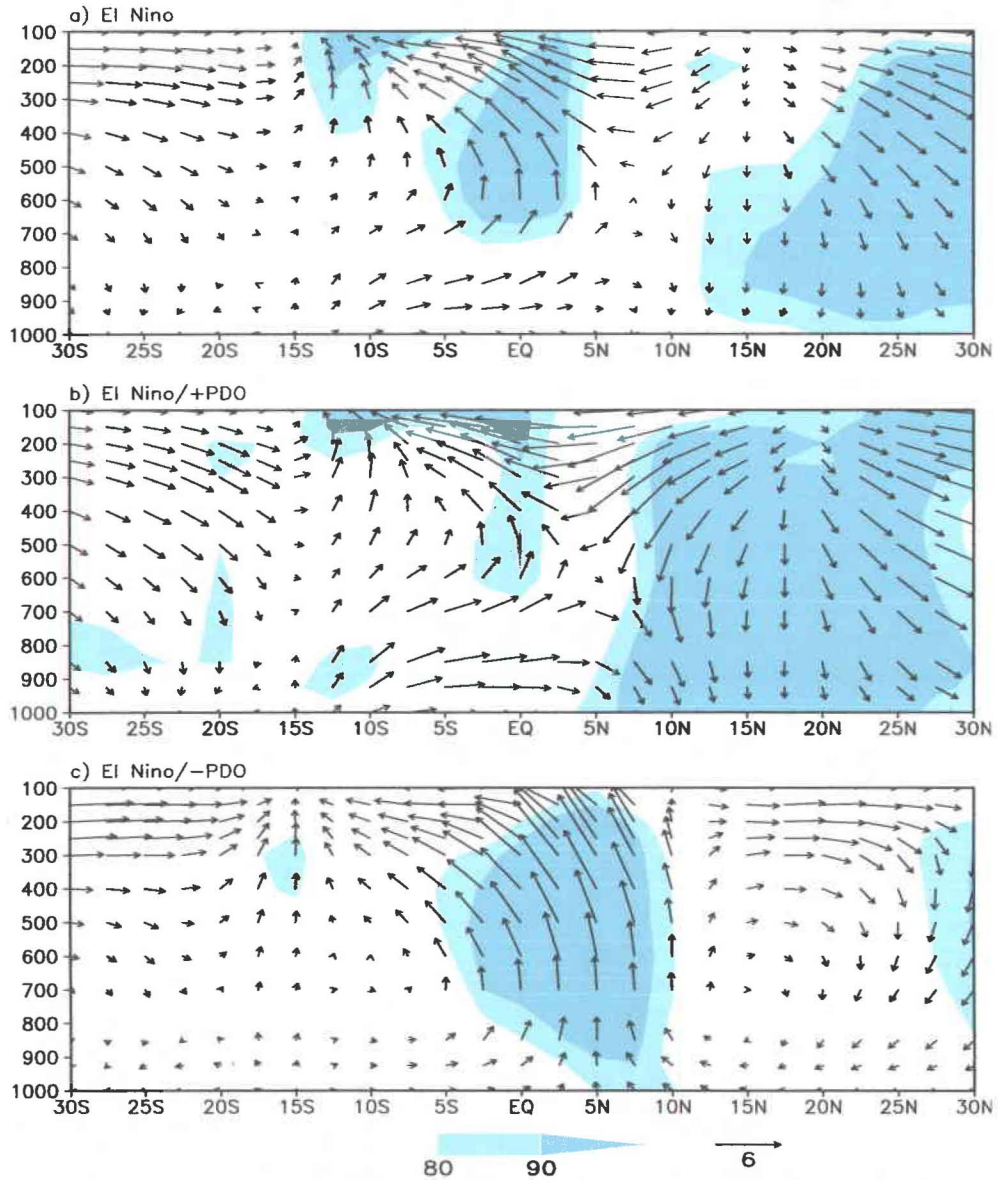
Fig. 23. Winter north-south vertical circulation anomalies: (a) El Niño, (b) El Niño/+PDO, and (c) El Niño/-PDO. Latitude-height section of meridional wind and negative pressure vertical velocity (V,-ω) is averaged over 165°W-150°W. Shading is nonparametric Mann-Whitney test based on the vertical velocity at the 80% and 90% levels. The unit vector in the horizontal direction is 6 m/s while that in the vertical direction is 0.03 Pa/s.
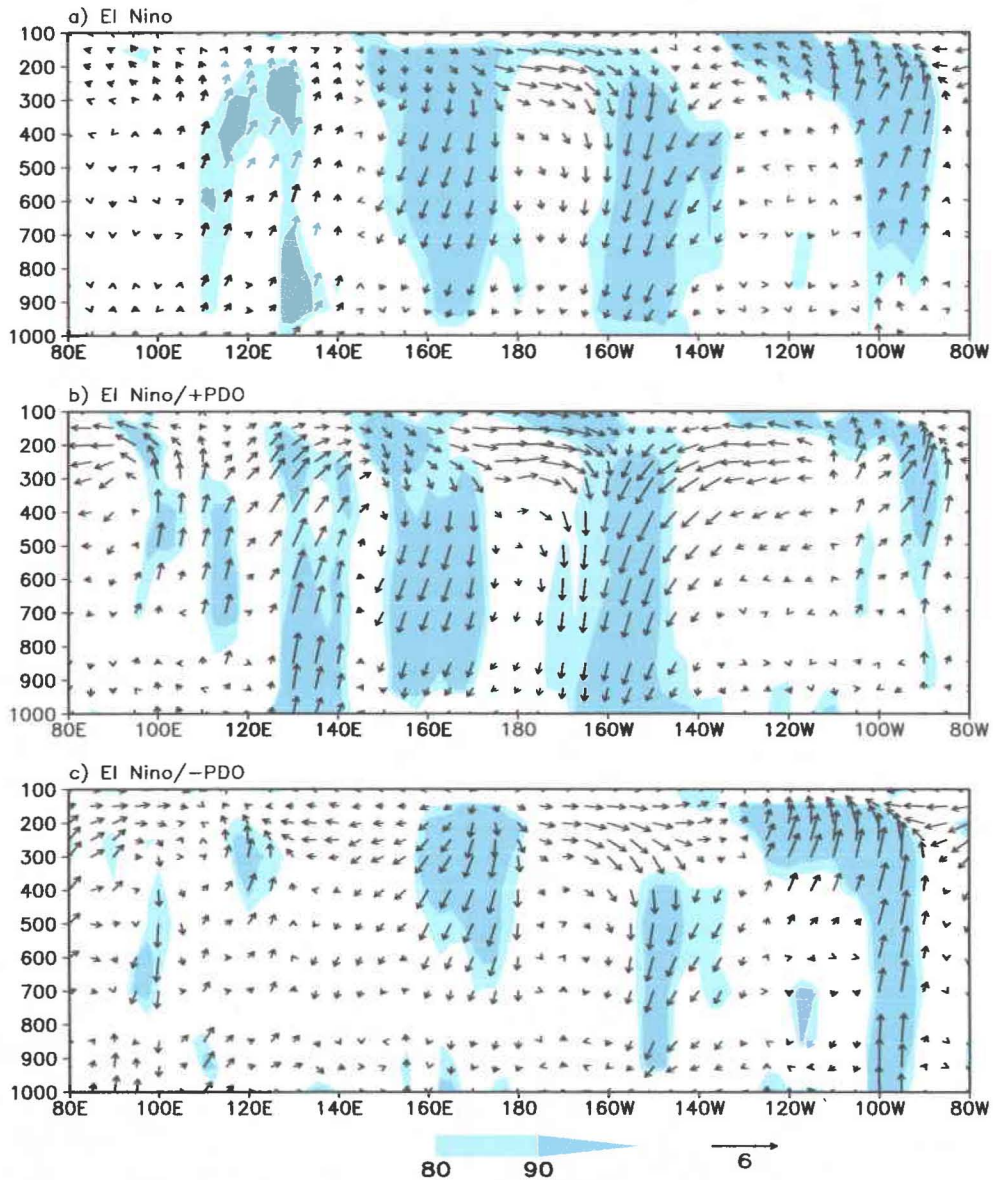
Fig. 24. Winter east-west vertical circulation anomalies: (a) El Niño, (b) El Niño/+PDO, and (c) El Niño/-PDO. Longitude-height section of zonal wind and negative pressure vertical velocity (U,-ω) is averaged over 15°N-25°N. Shading is nonparametric Mann-Whitney test based on the vertical velocity at the 80% and 90% levels. The unit vector in the horizontal direction is 6 m/s, while that in the vertical direction is 0.03 Pa/s.
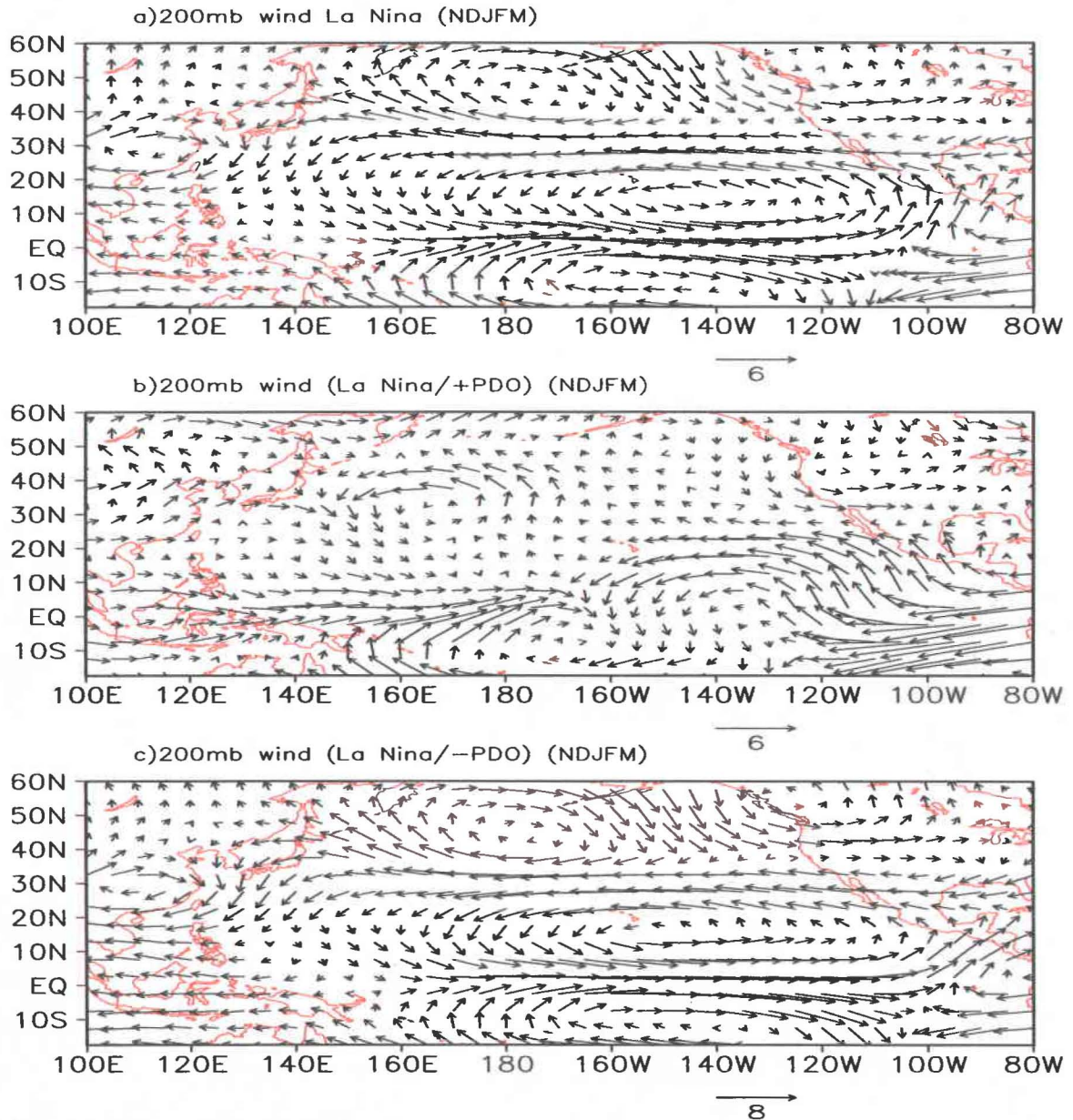
Fig. 25. Winter 200mb wind anomalies (vectors): (a) La Niña, (b) La Niña/+PDO, and (c) La Niña/-PDO. The unit for the wind vectors is m/s.
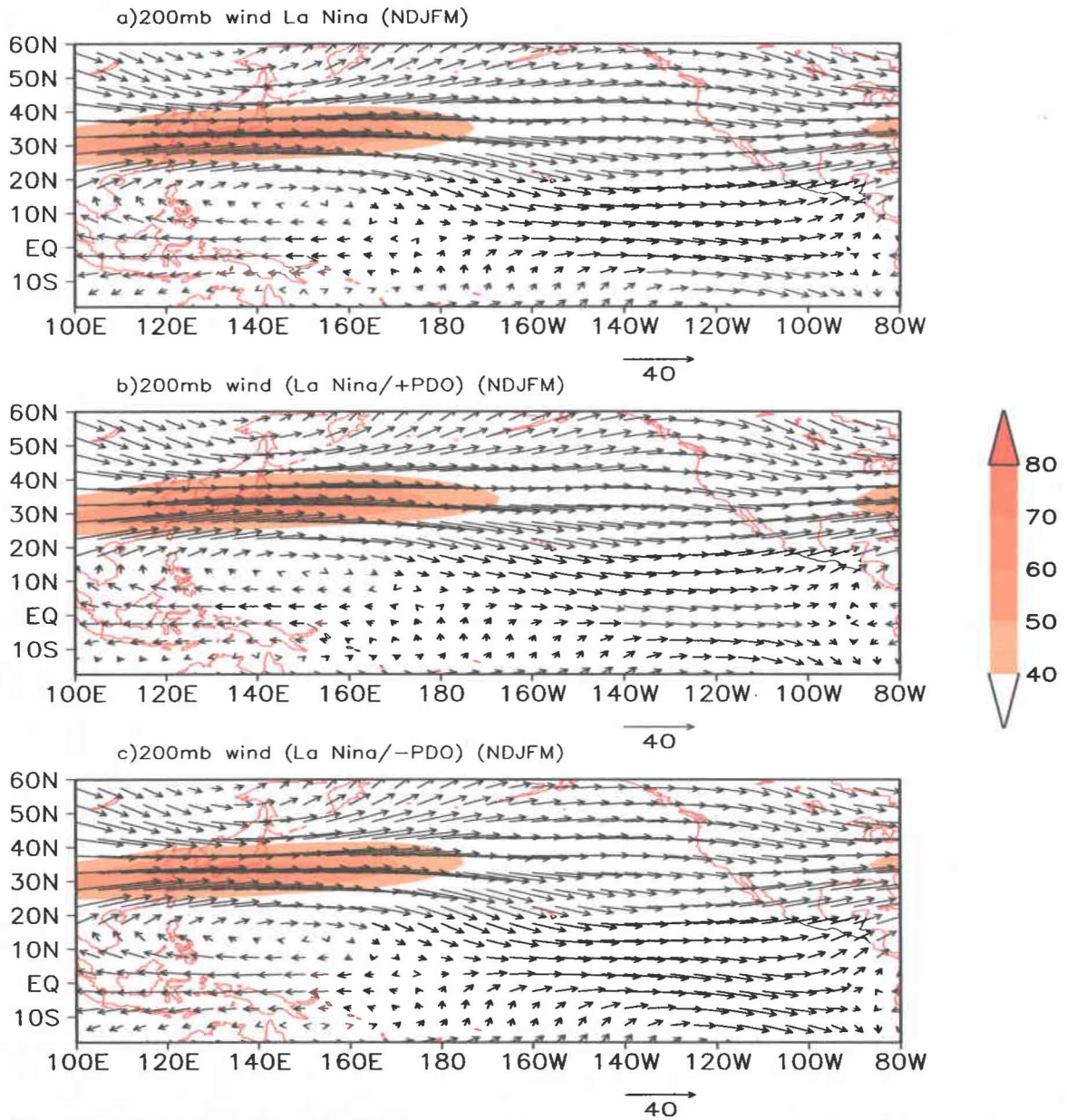
Fig. 26. Winter 200mb wind filed (vectors) for: (a) La Niña, (b) La Niña/+PDO, and (c) La Niña/-PDO. Area with wind speed greater than 40 m/s is shaded.
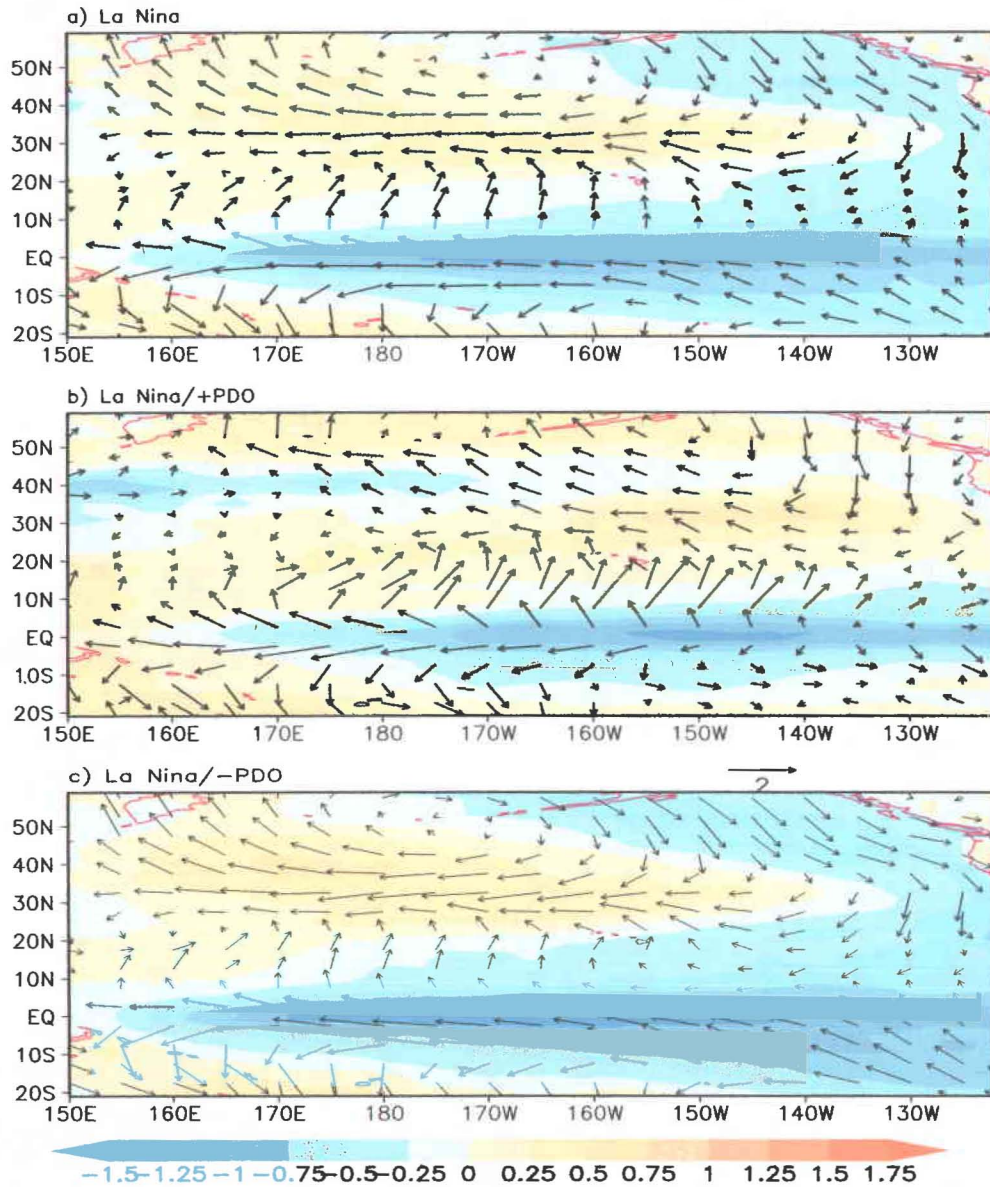
Fig. 27. Winter sea surface temperature and surface wind (vectors) anomalies: (a) La Niña, (b) La Niña/+ PDO, and (c) La Niña/-PDO. The unit for SST is °C, while the unit for the wind vectors is m/s.
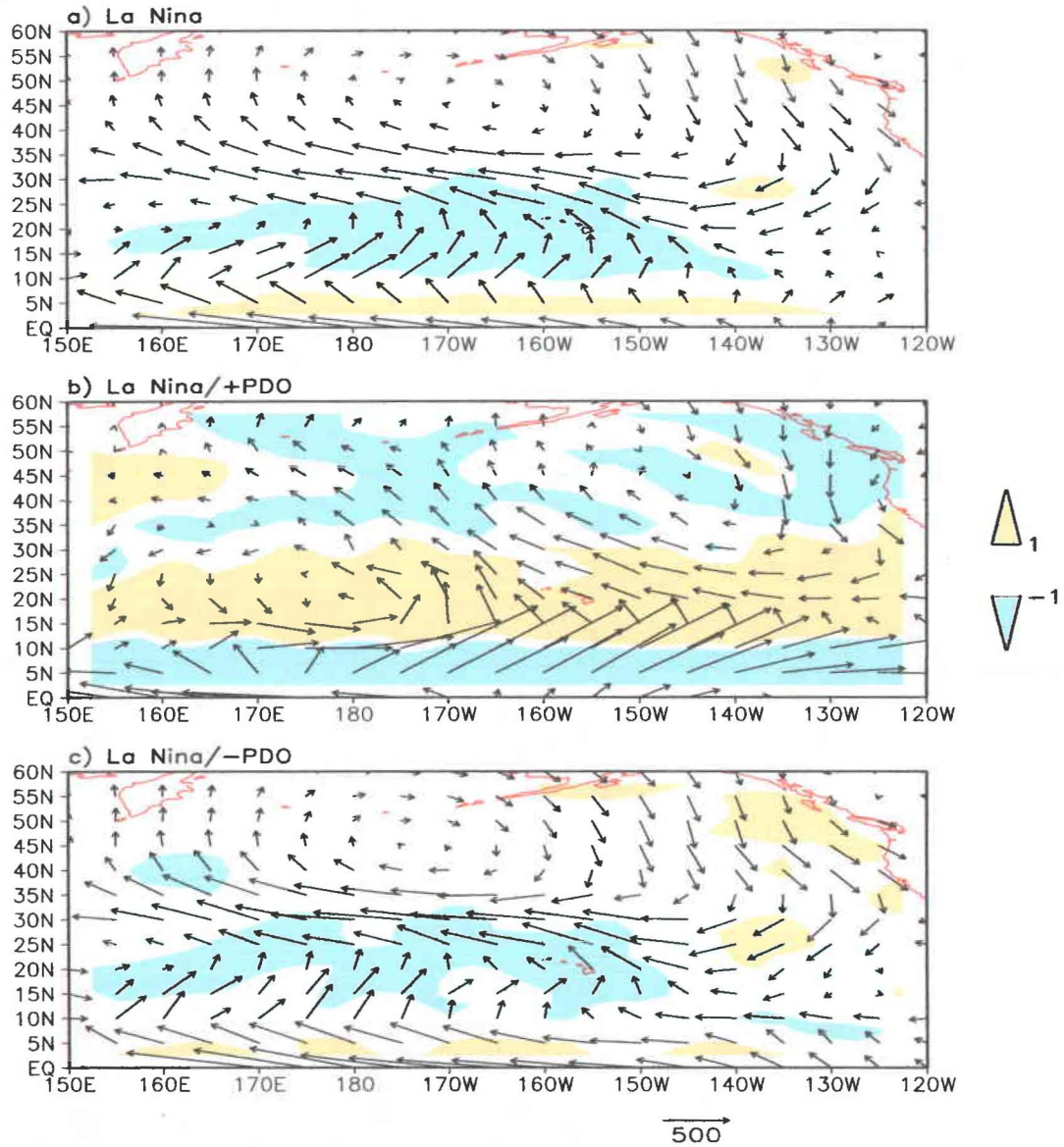
Fig. 28. Winter vertically integrated moisture flux (qu,qv) (vectors) and moisture flux divergence D(Q) (shading) anomalies: (a) La Nina, (b) La Niña/+PDO, and (c) La Niña/-PDO. Values for D(Q) greater (less) than 1(-1) mm day^{-1} are shaded yellow (blue). The unit for flux is g (cm s)$^{-1}$.
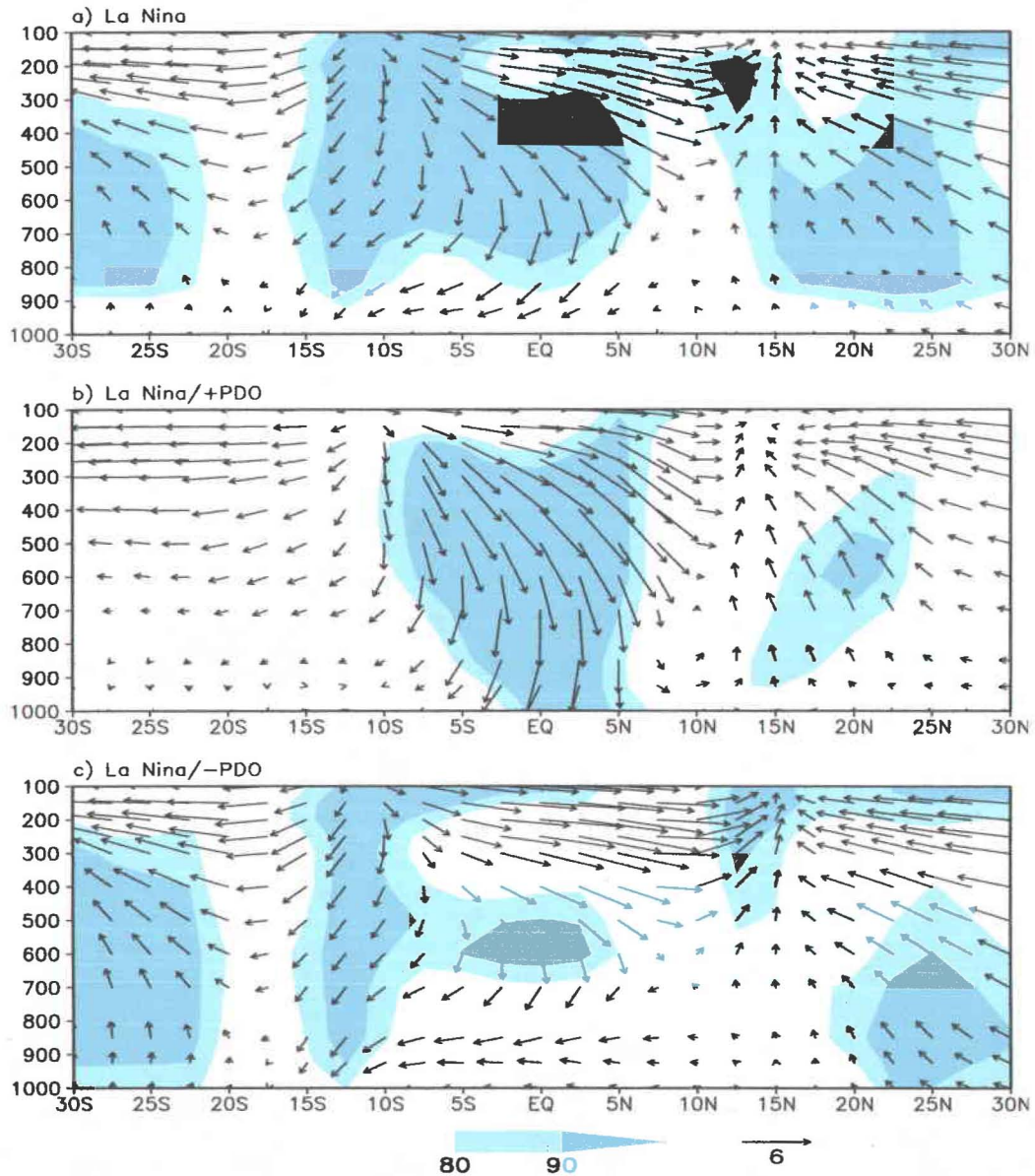
Fig. 29. Winter north-south vertical circulation anomalies: (a) La Nina, (b) La Niña/+PDO, and (c) La Niña/-PDO. Latitude-height section of meridional wind and negative pressure vertical velocity (V,-ω) is averaged over 165°W-150°W. Shading is nonparametric Mann-Whitney test based on the vertical velocity at the 80% and 90% levels. The unit vector in the horizontal direction is 6 m/s while that in the vertical direction is 0.03 Pa/s.
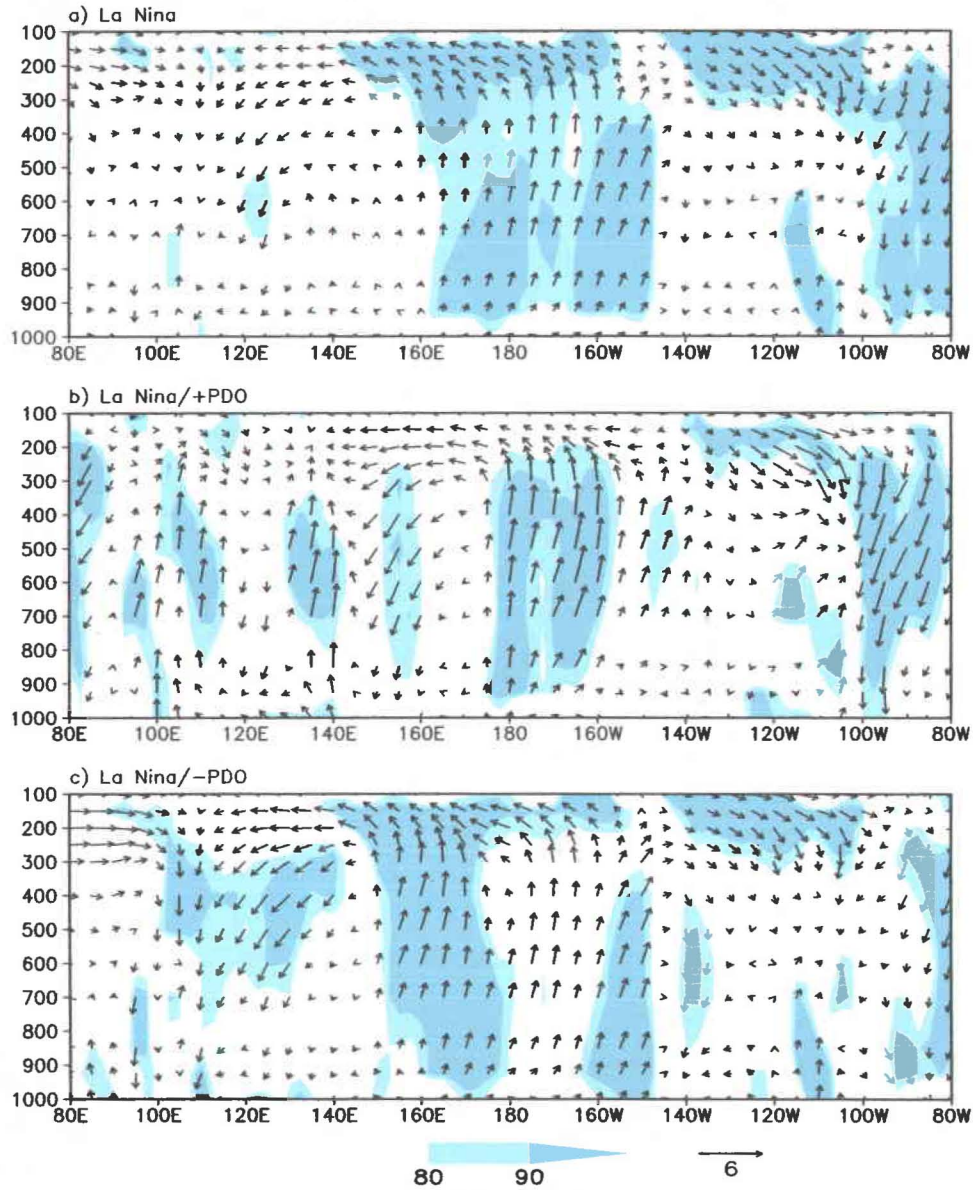
Fig. 30. Winter east-west vertical circulation anomalies: (a) La Nina, (b) La Niña/+PDO, and (c) La Niña/-PDO. Longitude-height section of zonal wind and negative pressure vertical velocity (U,-ω) is averaged over 15°N-25°N. Shading is nonparametric Mann-Whitney test based on the vertical velocity at the 80% and 90% levels. The unit vector in the horizontal direction is 6 m/s, while that in the vertical direction is 0.03 Pa/s.
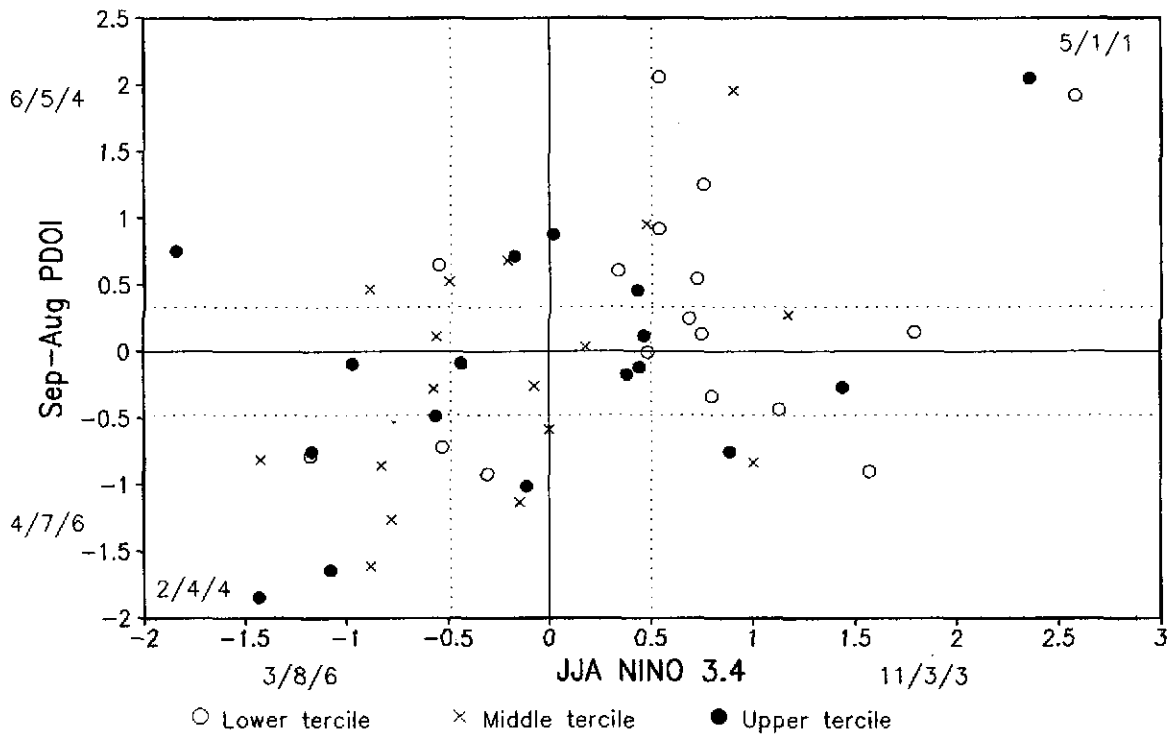
71

Fig. 31. Scatterplots for NDJFM precipitation against antecedent JJA Niño 3.4 and Sep-Aug PDOI values. Open circles indicate precipitation values in the lower tercile, and closed circles denote precipitation values in the upper tercile. See text for detailed explanation of the trios of numbers labeled.